Chapter 3 Sol-Gel-Derived $Zn_{(1-x)}Mg_xO$ Thin Films Used as Active Channel Layer of Thin-Film Transistors

3.0 Preface

Sol-gel derived *n*-type $Zn_{(1-x)}Mg_xO$ ($x = 0 - 0.45$) thin films and thin-film transistors (TFTs) with active channel layers made of the films were investigated. The films were prepared at 500℃. The effects of Mg doping on the crystallinity, optical transparency, grain size, and charge-carrier concentration (n) of the films were examined. The Fermi level of the films, as derived from the temperature dependence of n, was ~0.12 eV below the conduction band. The donor concentration and donor level (E_d) were derived by a curve fitting method based on the electrical neutrality condition. E_d was found to be about 0.3 eV below the conduction band. The composition dependence of the TFT output characteristics was interpreted and correlated to the width of the depletion region adjacent to the grain boundaries. When the grains were almost depleted at $x = 0.2$, the TFT showed an enhancement mode and an on/off ratio of 10^6.

3.1 Introduction

ZnO is a normally *n*-type compound semiconductor with a wide band

gap of 3.2 eV at room temperature, which has been used in varistors, transparent conductors [1,2], light-emitting diodes and UV-laser-emitting devices [3,4]. Recently, ZnO thin films, prepared by pulsed laser deposition (PLD) [5,6] or sputtering [7,8], have been used as the active channel layers (ACLs) of transparent thin film transistors (TFTs), and current on/off ratios in the range of $10^5 - 10^7$ were obtained. Besides the above fabrication processes involving vacuum techniques, the chemical solution deposition (CSD) process has been proved as an effective way to prepare ZnO ACLs in TFTs with an on/off ratios in the range of $10^3 - 10^7$, the annealing temperatures of which were above 700℃ [9,10]. Conventional TFTs, where the ACL is made of thin-film amorphous silicon or polycrystalline silicon by chemical vapor deposition (CVD), are fabricated on glass substrates, which are mechanically stable up to around 600℃. For applications of ZnO TFTs to the driving circuits of large flat-panel displays, CSD, a promising low-cost process, with a lower annealing temperature is highly desirable.

It has been demonstrated that the performance of ZnO TFTs is strongly dependent on the fabrication techniques and processing parameters used, which influences the electrical properties of TFTs, particularly the electron transport in the polycrystalline ZnO ACL. Previous theoretical studies [11,12] have illustrated that the polycrystalline film characteristics, such as grain size, donor concentration in the grains, and strap charge density at the grain boundary surfaces, primarily determines the current-voltage characteristics of the TFT. In addition to the process control, impurity doping has been frequently used to alter the electronic properties and

microstructures of ZnO, as in the case of varistors. It provides a means for modulating the ACL characteristics. In this work, we studied the effects of Mg doping on the performance of a ZnO TFT, where $Zn_{(1-x)}Mg_xO$ ACLs were prepared by CSD at a low annealing temperature of 500℃. A large Mg solubility has been found in ZnO epitaxial films prepared by PLD and CSD [13,14], where the investigations were focused on their optical properties. The high solubility, due to the similarity of the ionic radii of Mg and Zn, provided this research with an extensive range of *x* for study.

3.2 Experiment

A mixture of zinc acetate 2-hydrate [$Zn(CH_3COO)_2 \cdot 2H_2O$] and magnesium chloride anhydrous [$MgCl_2$], used as the sol-gel precursor, was dissolved in 2-methoxyethanol and monoethanolamine (MEA) and stirred at 60℃ for 30 min to form the sol-gel solution. The ratio of concentration of the metal ions in the solution is [Zn]: [Mg] = (1-*x*): *x*, where *x* was varied from 0 to 0.45. The total concentration of the metal ions was maintained at 0.75 moles per liter. The $Zn_{(1-x)}Mg_xO$ films were deposited on substrates by dip coating in the solution three times. The coated films were then dried at 400℃ for 30 min and annealed at 500℃ for 2 hr under an air atmosphere realizing a thickness of 0.1μm. The composition of the films was found to be consistent with that of the solution within 1% deviation, as verified with an inductively coupled plasma-atomic emission spectrometer (ICP-AES). The crystallinity of the films was examined by X-ray diffraction (XRD,

Siemens D5000) analysis with Cu $K\alpha$ radiation. The film surface morphology was observed by scanning electron microscopy (SEM, Hitachi S-4700) and atomic-force microscope (AFM, Digital Instruments Nanoscope III). X-ray photoelectron spectrometer (XPS) analysis was performed on an ESCLAB MKII using Mg $K\alpha$ ($h\nu$ = 1253.6 eV) as the exciting source. The dielectric constant of the films was measured from the capacitance of $Pt/Zn_{(1-x)}Mg_xO/Pt/SiO_2/Si$ with a HP 4284 A capacitance meter at 100 kHz. The temperature dependence of charge carrier concentration n of the films was measured in darkness by a capacitance-voltage (*C*-*V*) technique ($n = -2\left(q\varepsilon_s dC^{-2}/dV^{-1}\right)$) with a MOS structure ($Al/SiO_2/ZnO/Pt/SiO_2/Si$). The sample temperature can be varied up to 300℃ in a bias temperature stress (BTS) measurement system, which consisted of a Keithley 590 *C*-*V* Analyzer, a 595 *C*-*V* Quasi Meter, and a 230 Voltage Source.

The device structure of the $Zn_{(1-x)}Mg_xO$ TFT is of the bottom-gate type, as shown in Figure 3-1. Metal chrome was deposited and patterned on glass substrates as a bottom gate electrode. A gate insulator (SiO_2) with a thickness of 3000 Å was deposited by PECVD. Indium tin oxide (ITO) was used for the source and drain electrodes. Finally, the $Zn_{(1-x)}Mg_xO$ ACL, with a thickness, length, and width of 0.1 , 10, and 500 μm, respectively, was prepared by the methods mentioned above. The current-voltage (*I*-*V*) characteristics of the devices were measured in the dark with a semiconductor parameter analyzer (HP 4155A).

3.3 Results and Discussion

3.3.1 Film properties

The XRD spectra of the $Zn_{(1-x)}Mg_xO$ thin-films are shown in Figure 3-2, where the fraction x was varied from 0 to 0.45. The film structure formed in the wide region $x \leq 0.40$ was identified as hexagonal wurtzite ZnO, and a significant MgO cubic phase was detected at $x = 0.45$ by its (200) peak. The high solubility of MgO in ZnO films, possibly ranging from $x = 0.25$ to 0.33, was also reported by Ohtomo *et al*. [13] in their study of epitaxial $Zn_{(1-x)}Mg_xO$ films prepared by PLD. Even the thermodynamic solubility limit of MgO in ZnO has been reported to be less than 4 mol%, according to the phase diagram of the ZnO-MgO binary system [15], the solubility of Mg in ZnO thin films seems reveals much larger than that of solid solution. In addition, it is noted that the preferred (002) orientation of the films was strongly improved with increasing Mg content. Moreover, the lattice constant c of wurtzite $Zn_{(1-x)}Mg_xO$ were calculated, according to Bragg's law

$$2d \sin\theta = n\lambda \tag{3-1}$$

For hexagonal structure of ZnO, lattice constants a and c are given by

$$\frac{1}{d_{hkl}^2} = \frac{4}{3}\left(\frac{h^2 + hk + k^2}{a^2}\right) + \frac{l^2}{c^2} \tag{3-2}$$

With the first order approximation, $n = 1$:

$$\sin^2\theta = \frac{\lambda^2}{4}\left(\frac{4}{3}\frac{h^2 + hk + k^2}{a^2} + \frac{l^2}{c^2}\right) \tag{3-3}$$

For the (002) orientation at $2\theta \approx 34.42^{o}$, the lattice constant c was

calculated by

$$c = \frac{\lambda}{\sin\theta} \tag{3-4}$$

Typical transmission spectra, as displayed in Figure 3-3, show that Mg doping improved the transparency of the films. The $Zn_{(1-x)}Mg_xO$ films were highly transparent to visible light for all doped samples. In order to estimate the band gap energies of the $Zn_{(1-x)}Mg_xO$ thin films, we employed an $[\alpha h\nu]^2$ vs. $h\nu$ plot for the spectra to fit the data assuming an $\alpha^2 \propto (h\nu - E_g)$ relationship, where α is the absorption coefficient and $h\nu$ is the photon energy. Figure 3-4 shows the relative absorption coefficients and fitting results of $Zn_{(1-x)}Mg_xO$ thin films where *x* ranged from 0.00 to 0.30. Sharp absorption edges are clearly observed. The *c*-axis length and optical band gap are shown as a function of *x* in Figure 3-5. It is found that the lattice constant of *c*-axis decreased with higher Mg content, but the band gap energy increased with more Mg additives. This phenomenon has also been observed in other reports [16-19]. Since the ionic radii of Mg ions are slightly smaller than that of Zn ions (Mg^{2+}: 0.57 Å, Zn^{2+}: 0.60 Å) [20], it is considered that as more Mg ions were introduced into the ZnO thin films, Mg ions lodged themselves in an interstitial position, which leads to a decrease of the lattice constant. Moreover, the band gap energy of $Zn_{(1-x)}Mg_xO$ increased up to 3.60 eV for $0 \le x \le 0.30$. The effects of $Zn_{(1-x)}Mg_xO$ band gap increase on its physical properties are discussed in another section of this chapter.

The SEM and AFM images of un-doped ZnO films annealed at 400℃ to 600℃ are shown in Figure 3-6 and 3-7, respectively. It could be seen

that the morphologies of ZnO thin films derived from sol-gel method showed chain-like structure. The grain sizes of un-doped ZnO films have a slight increase with the elevated annealing temperature, and the grain size of all films were less than 100 nm. The influence of Mg dopants on the surface morphologies of $Zn_{(1-x)}Mg_xO$ films, which observed by SEM and AFM were displayed in Figure 3-8 and 3-9, respectively. It is also found that the chain-like structure of ZnO films was diminished by means of doping Mg. The grain growth of the films appeared to be enhanced by the addition of Mg. The average grain size L_g of the pure ZnO films was ~50 nm, and L_g ~ 100 nm for all the doped films. The porosity was observed in all sol-gel-derived $Zn_{(1-x)}Mg_xO$ films. Figure 3-10a shows the roughness of un-doped ZnO films annealed at temperatures ranged from 400℃ to 600℃. It could be observed that the roughness of un-doped ZnO films decreased with annealing temperature below 500℃, and the roughness increased when the temperature was more than 500℃. The roughness of ZnO films exhibited the lowest roughness annealed at 500℃ which might result from the optimized densification of the chain-like structure obtained at an annealing temperature of 500℃. Furthermore, Figure 3-10b displays the effects of Mg additives on the roughness of $Zn_{(1-x)}Mg_xO$ films annealed at 500℃. The roughness of the films was reduced with more Mg content, and this is due to the diminution of the chain-like structure by means of doping Mg ions.

The sol-gel-derived $Zn_{(1-x)}Mg_xO$ thin films were also characterized by

XPS to study the binding energy and chemical shift of the elements in the $Zn_{(1-x)}Mg_xO$ films. Figure 3-11 and 3-12 shows the XPS survey scan analysis of the un-doped ZnO and $Zn_{(1-x)}Mg_xO$ films, where x ranged from 0.10 to 0.40, respectively. Figure 3-11 displays that there are Zn, O, and C elements in the un-doped ZnO films. The detection of small amounts of carbon could be attributed to the residual precursor and reactant adsorbed on the surface. The two strong peaks located around 531 and 1022 eV, respectively, as shown in Figure 3-11 and 3-12 agree with the O 1s and Zn $2p_{3/2}$ binding energy for ZnO. Figure 3-12c shows the appearance of the Mg 2s peak when x = 0.30, and the Mg 2p peak appeared while the Mg content was elevated to x = 0.40, as shown in Figure 3-12d. Figure 3-13 shows XPS spectra of O 1s of $Zn_{(1-x)}Mg_xO$ thin films, where x ranged from 0.00 to 0.40. The typical O 1s peak in the surface could be fitted by two nearly Gaussian, centered at 530 and 531.4 eV, in the spectra of x = 0.00. The component on the low binding energy side of the O 1s spectrum at 530 eV is attributed to O^{2-} ions on wurtzite structure of hexagonal Zn^{2+} ion array, surrounded by Zn atoms with their full complement of nearest-neighbor O^{2-} ions [21-23]. In other words, the intensity of this component is the measure of the amount of oxygen atoms in a fully oxidized stoichiometric surrounding. The higher binding energy component located at 531.4 eV is usually attributed to the presence of loosely bound oxygen on the surface of the $Zn_{(1-x)}Mg_xO$ films, belonging to a specific species, e.g., $-CO_3$, adsorbed H_2O or adsorbed O_2 [24,25]. Figure 3-13 shows that the O 1s peak position shifted to the higher binding energy side when the Mg content was increased. This phenomenon indicates that the

number of oxygen atoms in higher Mg content of $Zn_{(1-x)}Mg_xO$ films must have increased. The additional oxygen atoms exist partially as Zn-O bonds and partially as free oxygen. Figure 3-14 shows the relative intensity of the O 1s peak as the function of the *x* values in $Zn_{(1-x)}Mg_xO$ films. It could be observed that the relative intensity of the O 1s peak increased with higher *x* values. The fast increase of relative intensity of the O 1s component with more Mg content reveals that the amount of zinc-oxygen bonding was increased as higher *x* values. Figure 3-15 displays the XPS spectra of Zn $2p_{3/2}$ of $Zn_{(1-x)}Mg_xO$ thin films, where *x* ranged from 0.00 to 0.40. The peak corresponding to Zn $2p_{3/2}$ shifted to higher binding energy side as higher Mg additives, which is indicative of more zinc atoms being bound to oxygen atoms [26]. From the XPS data, it is considered that the numbers of oxygen atoms were increased with more Mg dopants. Furthermore, the amount of bonding between oxygen and zinc were also increased by doping Mg ions. It indicates that the numbers of defects, including oxygen vacancies and interstitial zinc atoms, were diminished with higher *x* values in $Zn_{(1-x)}Mg_xO$ films. This finding is consistent with the photoluminescence (PL) observation of $Zn_{(1-x)}Mg_xO$ thin films [17]. From the PL spectra, the broad deep-level emissions resulted from oxygen and zinc defects were eliminated by doping Mg ions. Therefore, the $Zn_{(1-x)}Mg_xO$ thin films exhibited fewer defects such as oxygen vacancies and interstitial zinc atoms when Mg was introduced into the films. Figure 3-16 shows the XPS spectra of Zn $3p_{1/2}$ and Mg 2s of $Zn_{(1-x)}Mg_xO$ thin films, which *x* ranged from 0.10 to 0.40. The peaks at 90.6 and 87.6 eV corresponding to Zn $3p_{1/2}$ and Mg 2s, respectively, have no significantly shift.

The charge carrier concentration *n* of various $Zn_{(1-x)}Mg_xO$ films was measured at temperatures ranging from 25 to 125℃. The films were fabricated with a MOS structure with a top electrode of diameter 0.35 mm, with which the *C*-*V* curves were measured and *n* was evaluated. Regarding the measurement of carrier concentration *n* from the slope of C^{-2} vs. *V* curves in the MOS structure, an extensive discussion was presented in Ref. [27]. It was emphasized that the differential capacitance-voltage profiling technique determines the majority carrier concentration not the doping concentration because the charges that actually move in response to the ac voltage are the mobile charges, not the ions. If the emission and capture processes of the donors can follow the ac voltage variation, the total charge response to ac voltage would be proportional to sum of the mobile charges concentration and unionized donors concentration. Because the sum is equal to the doped donor concentration, which is constant, the charge carrier concentration measured from the slope of C^{-2}-*V* curves would be independent of temperature, but it is not our case. The related discussion can be found in Ref. [28]. The ionized donors in the depletion region do have an effect on the static capacitance *Q*/*V*, but have no effect on the dynamic capacitance *dQ*/*dV*, which is *C*-*V* measurement focused on.

Typical results are shown in Figure 3-17. Each *n* value presented here is the average of measurements taken from five randomly selected electrodes. The associated standard deviation of the *n* value was found to be about 0.3-0.9% for $x \leq 0.25$, and around 2% for $x = 0.4$. At room temperature, $n \sim 10^{16}$-10^{17} /cm^3, and it increased around 4-5-fold at the temperature of 125℃, indicating that the donors were deep-level type and

partially ionized in this temperature range. In the *C-V* measurement the MOS was biased at a dc voltage *V* plus a sinusoidal ac voltage (1 MHz). The voltage *V* causes the formation of a depletion region and energy band bending. The wide band gap of (Zn,Mg)O allows us to neglect the interference of minority carriers generated in the deep depletion region. For samples with a uniform distribution of deep-level donors, when the ac voltage oscillation frequency is sufficiently high, the partially ionized donors located at the edge of the depletion region will not be able to emit or capture electrons synchronously with the voltage variation. In such a case, the constant slope of the C^{-2} vs *V* curve will give us the mobile charge carrier concentration *n*, which will be a strong function of temperature with definite thermal activation energy. The observed temperature dependence of the concentration *n* indicated that our (Zn,Mg)O samples are consistent with the above conditions.

Since the ZnO grain boundaries, which usually have a high density of trap states, were negatively charged, a double depletion layer (associated with a double Schottky barrier) formed adjacent to each grain boundary. If the depleted region is a fraction (*1-r*) of the grain volume v_g, the un-depleted central region has a volume equals to rv_g, in which mobile charges of local concentration n_g stay. The parameter *r* characterized the un-depleted region size and depended on doping level and film processing conditions, as shown in Figure 3-18. The *n* value obtained from the *C-V* measurements actually represents the concentration averaged over the grains in the films, hence $n_g = n/r$. In the central region n_g follows the

relation:

$$n_g = N_C \exp\left(\frac{E_F - E_C}{kT}\right)$$

or
$$\ln\left(\frac{n}{T^{3/2}}\right) = \ln\left(\frac{2(2\pi k)^{3/2}}{h^3} \times r\, m_e^{3/2}\right) + \frac{E_F - E_C}{kT} \tag{3-5}$$

where $N_c = 2(2\pi m_e kT/h^2)^{3/2}$, assuming that the Fermi level E_F is under the beneath of the conduction band $E_C \equiv 0$ by more than kT [29]. According to eq. (3-5), the measured charge carrier concentration in the form $\ln(n/T^{3/2})$ is plotted versus $1/kT$ in Figure 3-19 to evaluate the E_F and $r\,m_e{}^{3/2}$ values from the slope and extrapolated intercept. The results are listed in Table 3-1, where the electron effective mass m_e was in units of free electron mass. For each composition the Fermi level found in the temperature range is constant.

The condition for electrical neutrality in the central region is expressed as

$$n_g + N_a = N_d - n_d \tag{3-6}$$

where N_a, N_d, and n_d are the densities of acceptors, donors, and nonionized donors, respectively. To simplify the following analysis, here we assumed that the acceptor levels were fully filled. From the relation $N_a = (1-f)N_d$, where f is a constant, and

$$n_d = \frac{N_d}{1 + \frac{1}{2}\exp(E_d - E_F)/kT} \tag{3-7}$$

where E_d is the donor energy level, [29] we have

$$\ln\left[2\left(f-\frac{n}{rN_d}\right)^{-1}-2\right]=(E_d-E_F)/kT \qquad (3\text{-}8)$$

The highly linear curves shown in Figure 3-19 made it possible to express the temperature dependence of n continuously as an analytic function $n=n_oT^{3/2}\exp(E_F/kT)$, for each Mg dosage, within the temperature range investigated. With this analytic type of function, we found by the curve fitting method that only one set of f, rN_d, and E_d-E_F values (listed in Table 3-1) satisfies eq. (3-8), as shown in Figure 3-20. The straightness of the fitted line is sensitive to the f value chosen. It was found that (1- f) ≤ 10^{-4} for all the compositions, i.e., the acceptor density N_a is negligible compared with the donor density. In addition, an appropriately selected rN_d value will make the fitted line extrapolate through the origin. The experimental data of n (Figure 3-19), instead of the analytic function, were used in eq. (3-8), the results are marked in Figure 3-20, showing a good consistency with the fitted curves.

Previous studies of deep-level transient spectroscopy on the electrical characterization of ZnO have shown the presence of several deep-level traps. Among them, L_2, with a level situated 0.26 [30] ~ 0.29 eV [31] below the conduction band, was found in both single-crystal and polycrystalline ZnO and was proposed to be either the zinc interstitial [30] or an oxygen vacancy [31]. The donors in the ZnO films (E_d = 0.27 eV for x = 0) presumably corresponded to the defect L_2. The value of rN_d obtained is of

the order of $10^{20}/cm^3$, indicating a high density of donors, which might be due to the low-temperature processing of the films.

For the case of $x = 0$, $r m_e^{3/2} = 0.74$. Since $r \leq 1$, hence $m_e^{3/2} \geq 0.74$, or $m_e \geq 0.82$. The recently reported value of the electron effective mass, *Me*, of bulk $Zn_{(1-x)}Mg_xO$ with $x = 0$, 0.05, 0.10, and 0.20, are 0.38, 0.46, 0.73, and 1.56, respectively [32]. The normalized ratio among them is 1: 1.21: 1.92: 4.1, which reveals the effect of increasing Mg doping on the effective mass. For the same Mg dosage, the effective mass m_e of our films is expected to be larger than the reported *Me*, as evidenced by the case of $x = 0$, because of their distinct microstructures. The mobile electrons suffer much more severe scattering in our films due to the size effect and the small grains. The shorter mean free path may lead to considerable increases in the density of states in the conduction band and the effective mass [33]. The microstructure effect may be expressed approximately as $m_e = c\, M_e$ for those films and bulk samples of the same doping, where c is a constant larger than one. The series of $r m_e^{3/2}$ values (Table 3-1), like the *Me* series, can be normalized as a ratio, 1: 0.91: 0.61: 0.17, which is equal to the $r M_e^{3/2}$ series ratio after the common factor c is cancelled out. Substituting the *Me* series ratio into we obtain the r series ratio as 1: 0.68: 0.226: 0.021, as listed in Table 3-1. The decreasing ratio indicates that the size of non-depleted central region in the grains of $Zn_{(1-x)}Mg_xO$ films decreases with Mg dosage and become negligible as the doping level reaches $x = 0.2$, corresponding to the almost depleted grains. In a similar way, for the r series ratio, the series of rN_d values (Table 3-1) gave the normalized ratio

of N_d as 1: 1.3: 2.7: 8.2. This ratio implies that the Mg doping increased the donor density as well as the trap-state density at the grain boundaries, which resulted in the trapping of more charge carriers and the expansion of the depletion region in the grains.

The increase of band gap E_g as well as donor activation energy E_d with Mg doping might be explained qualitatively as following. The increase E_g means that it requires more energy to excite the valence electrons to conduction band, indicating that Mg ions enhance the bonding of valence electrons to the ions on the crystal lattice. The donor level was presumably identified with L_2, which might be the zinc interstitials or the oxygen vacancies. The defects of both possible types are immediately surrounded by the doped Mg ions; the enhanced bonding force may apply to the elections on the donors so that E_d increases too. The other possible explanation is as follows. Since the depletion region in the grain increases with Mg dosage, the electric field in the grain boundary will increase with and then enhance the activation energy of donors due to the Stark effect. However, the activation energy was derived from the temperature dependence of the carrier concentration, which in turn was resulted from the ionization of donors in the un-depleted region, where it is electrical neutral. The high field of the grain boundary would not affect the donors in the neutral region. The electrical behaviors of deep-level donors or acceptors have been an interesting, but difficult problem, even for theoreticians. It seems hard to provide a sound explanation based on the current data. That is the reason why we leave the topic untouched.

In the composition range x = 0.25~0.40, the MgO dopant effect on the charge carrier concentration n became saturated (see Figure 3-19). The doping x = 0.25 might correspond to the solubility margin of MgO in ZnO, beyond which no more Mg could be dissolved, and N_D and n became constant. This is consistent with the results of Ref. [13]. A minor precipitate of the MgO phase might begin to form in the films at around x = 0.25, but was not detectable until x = 0.45 in the current XRD study.

3.3.2 TFT characteristics

The drain current-drain voltage (I_D-V_D) curves of the un-doped ZnO-TFT samples, as shown in Figure 3-21a, exhibited typical normally-on features and poor saturation drain current. The output characteristics of $Zn_{(1-x)}Mg_xO$-TFTs, where x = 0.05 and 0.10, exhibited similar features with un-doped ZnO TFT (not shown here). Figure 3-21b shows the drain current-gate voltage characteristics of the un-doped ZnO TFT, which depicted that the device exhibited an on/off ratio less than 10. Figure 3-22a and b display the output and output characteristics of the $Zn_{(1-x)}Mg_xO$-TFT which x = 0.20, respectively. Compared to the un-doped ZnO TFT, the drain current decreased with the increasing Mg content until x = 0.20, where the output characteristics changed to those of an n-channel enhancement mode and a clear saturation current behavior was observed. Even the on-state current of x = 0.20 slightly degraded compared to the un-doped ZnO TFT, the off-state current of the former has a significantly depression that leads to a high current modulation of more than 10^6.

The effects of Mg doping on the electrical properties of the polycrystalline ACL, which determined the performance of the TFT, were ascribed to the variation of the depletion region within the grains of the $Zn_{(1-x)}Mg_xO$ films. The correlation of the film properties, particularly the parameter r, with the device characteristics can be rationalized in the same way, as proposed by the recent theoretical study on the ZnO-TFTs [11]. If the trap states at the grain boundaries were sufficiently dense to trap most of the charge carriers in the grains, the potential profile of the double Schottky barriers at each grain boundary tended to overlap and resulted in a wholly depleted and highly resistive ACL. Such a TFT would be normally off and operate in an enhancement mode. The reverse of the above condition would lead to a more conductive ACL and a normally on TFT in the depletion mode. Consequently, the smallest r (or $r_{ub} = 0.02$) found at $x = 2.0$ corresponded to an almost depleted ACL with the best TFT performance in our study.

For the samples of $x \geq 0.25$, the drain current was abnormally high and the gate voltage failed to control the drain current (Figure 3-23). The degradation of the output characteristics indicated the breakdown of double Schottky barriers. The marked change in the physical properties of the grain boundaries in the films of high Mg content might be correlated with the tiny MgO phase, which presumably precipitated on the grain boundaries when the MgO solubility limit $x = 0.25$ was approached. The device characteristics of $Zn_{(1-x)}Mg_xO$-TFTs were summarized in Table 3-2. The saturation mobility (μ_{sat}) and threshold voltage (V_{th}) was calculated from the slopes and intercepts of $\sqrt{I_D} - V_G$ plots at V_D = 100 V,

respectively. As shown in Table 3-2, the μ_{sat} decreased with higher *x* values due to the Mg impurities acted as scattering centers for carrier transportation.

3.4 Conclusion

Sol-gel-derived *n*-type $Zn_{(1-x)}Mg_xO$ (x= 0~0.45) thin films and thin-film transistors (TFTs) with active channel layers made of the films have been prepared and investigated in this study. The Mg doping effectively increased the optical transparency, grain size, and densities of charge carriers, donors, and grain-boundary trap states of the films. The donor level of the ZnO films is found to be 0.27 eV below the conduction band. It is identified with the previously reported deep-level defect L_2, either an oxygen vacancy or the zinc interstitial. The depletion region in the grains increased with amount of Mg doping and resulted in almost depleted grains in the active channel layers at x = 0.2, where the TFT showed an enhancement mode and an on/off ratio of 10^6. The estimated solubility of MgO in ZnO is around x = 0.25, at which a minor precipitate of the MgO phase presumably begin to precipitate on the grain boundaries. That resulted in a saturated charge carrier concentration and degraded TFT performance.

References

[1] T. Minami, *Mater. Res. Bull.*, **25** 38 (2000).

[2] T. J. Coutts, D. L. Young and X. Li, *Mater. Res. Bull.*, **25** 58 (2000)

[3] R. F. Service: *Science*, **276** 895 (1997).

[4] P. Yu, Z. H. Tang, G. K. Wong, M. Kawasaki, A. Ohtomo, H. Koinuma and Y. Segawa: *Solid State Commun.*, **103** 459 (1997).

[5] S. Masuda, K. Kitamura, Y. Okumura, S. Miyatake, H. Tabata and T. Kawai: *J. Appl. Phys.*, **93** 1624 (2003).

[6] J. Nishii, F. M. Hossain, S. Takagi, T. Aita, K. Saikusa, Y. Ohmaki, I. Ohkubo, S. Kishimoto, A. Ohtomo, T. Fukumura, F. Matsukura, Y. Ohno, H. Koinuma, H. Ohno and M. Kawasaki, *Jpn. J. Appl. Phys.*, **42** L347 (2003).

[7] R. L. Hoffman, B. J. Norris and J. F. Wager, *Appl. Phys. Lett.*, **82** 733 (2003).

[8] P. F. Carcia, R. S. McLean, M. H. Reilly and G. Nunes, Jr., *Appl. Phys. Lett.*, **82** 1117 (2003).

[9] Y. Ohya, T. Niwa, T. Ban and Y. Takahashi, *Jpn. J. Appl. Phys.*, **40** 297 (2001).

[10] B. J. Norris, J Anderson, J. F. Wagner and D. A. Keszler, *J. Phys. D.*, **36** L107 (2003).

[11] F. M. Hossain, J. Nishii, S. Takagi, A. Ohtomo, T. Fukumura, H. Fujioka, H. Ohno, H. Koinuma and M. Kawasaki, *J. Appl. Phys.*, **94** 7768 (2003).

[12] J. Levinson, F. R. Shepherd, P. J. Scanlon, W. D. Westwood, G. Este and M. Rider, *J. Appl. Phys.*, **53** 1193 (1982).

[13] A. Ohtomo, M. Kawasaki, T. Koida, K. Masubuchi, H. Koinuma, Y. Sakurai, Y. Yoshida, T. Yasuda and Y. Segawa, *Appl. Phys. Lett.*, **72** 2466 (1998).

[14] D. Zhao, Y. Liu, D. Shen, Y. Lu, J. Zhang and X. Fan, *J. Appl. Phys.*, **90** 5561 (2001).

[15] J. F. Saver, Fred L. Katnack, and F. A. Hummel, *J. Electrochem. Soc.*, **106** 960 (1959).

[16] A. K. Sharma, J. Narayan, J. F. Much, C. W. Teng, C. Jin, A. Kvit, R. M. Kolbas, and O. W. Holland, *Appl. Phys. Lett.*, **75** 3327 (1999).

[17] F. K. Shan, B. I. Kim, G. X. Liu, Z. F. Liu, J. Y. Sohn, W. J. Lee, B. C. Shin, and Y. S. Yu, *J. Appl. Phys.*, **95** 4772 (2004).

[18] S. Muthukumar, J. Zhong, Y. Chen, Y. Lu, and T. Siegrist, *Appl. Phys. Lett.*, **82** 742 (2003).

[19] A. Ohtomo, M. Kawasaki, T. Koida, K. Masubuchi, H. Koinuma, Y. Sakurai, Y. Yoshida, T. Yasuda, and Y. Segawa, Appl. Phys. Lett., **72** 2466 (1998).

[20] R. D. Shannon, Acta Crystallogr., Sect. A: Cryst. Phys., Diffr., Theor. Gen. Crystallogr. **32** 751 (1976).

[21] R. Cebulla, R. Weridt, and K. Ellmer, *J. Appl. Phys.*, **83** 1087 (1998).

[22] T. Szorenyi, L. D. Laude, I. Bertoti, Z. Kantor, and Z. Geretovszky, *J. Appl. Phys.*, **78** 6211 (1995).

[23] L. K. Rao, and V. Vinni, *Appl. Phys. Lett.*, **63** 608 (1993).

[24] S. Major, S. Kumar, M. Bhatnagar, and K. L. Chopra, *Appl. Phys. Lett.*, **40** 394 (1986).

[25] M. N. Islam, T. B. Ghosh, K. L. Chopra, and H. N. Acharya, *Thin*

Solid Films, **280** 20 (1996).

[26] W. G. Han, S. G. Kang, T. W. Kim, D. W. Kim, and W. J. Cho, *Appl. Surf. Sci.*, **245** 384 (2005).

[27] Dieter K. Schroder, Semiconductor Material and Device Characterization (Arizona State University, 1998), 2nd ed., Chap. 2.

[28] L. C. Kimerling, *J. Appl. Phys.*, **45** 1839 (1974)

[29] R. A. Smith: Semiconductors (Cambridge University Press, Cambridge, 1978) 2nd ed., Chap. 4. p. 92.

[30] A. Rohatgi, S. K. Pang, T. K. Gupta and W. D. Straub, *J. Appl. Phys.*, **63** 5375 (1988).

[31] F. D. Auret, S. A. Goodman, M. J. Legodi, W.E. Meyer and D. C. Look, *Appl. Phys. Lett.*, **80** 1340 (2002).

[32] D. J. Cohen, K. C. Ruthe and S. A. Barnett, *J. Appl. Phys.*, **96** 459 (2004).

[33] N. F. Mott and E. A. Davis: Electronic Processes in Noncrystalline Materials (Oxford University Press, Oxford, 1979) 2nd ed., Chap. 2, p. 9.

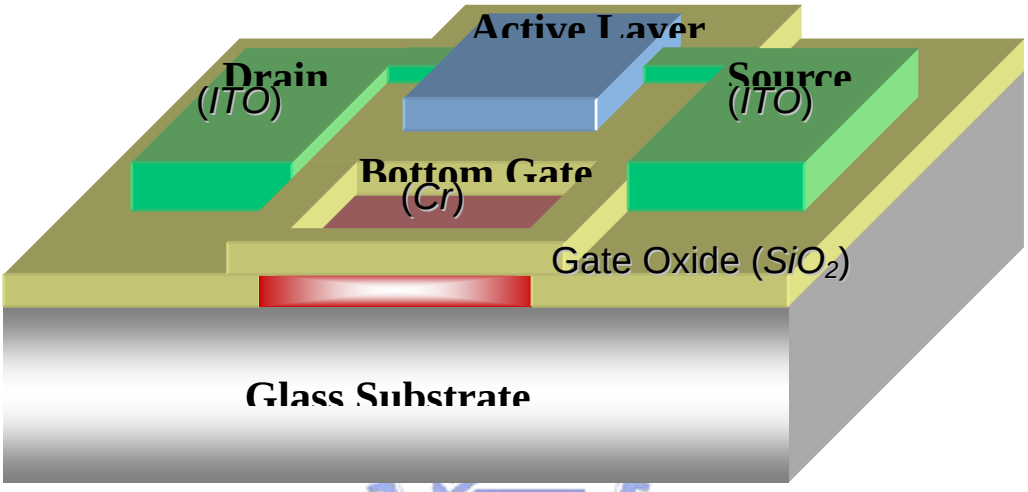

Figure 3-1 Schematic diagram of TFT using $Zn_{(1-x)}Mg_xO$ as active channel layer.

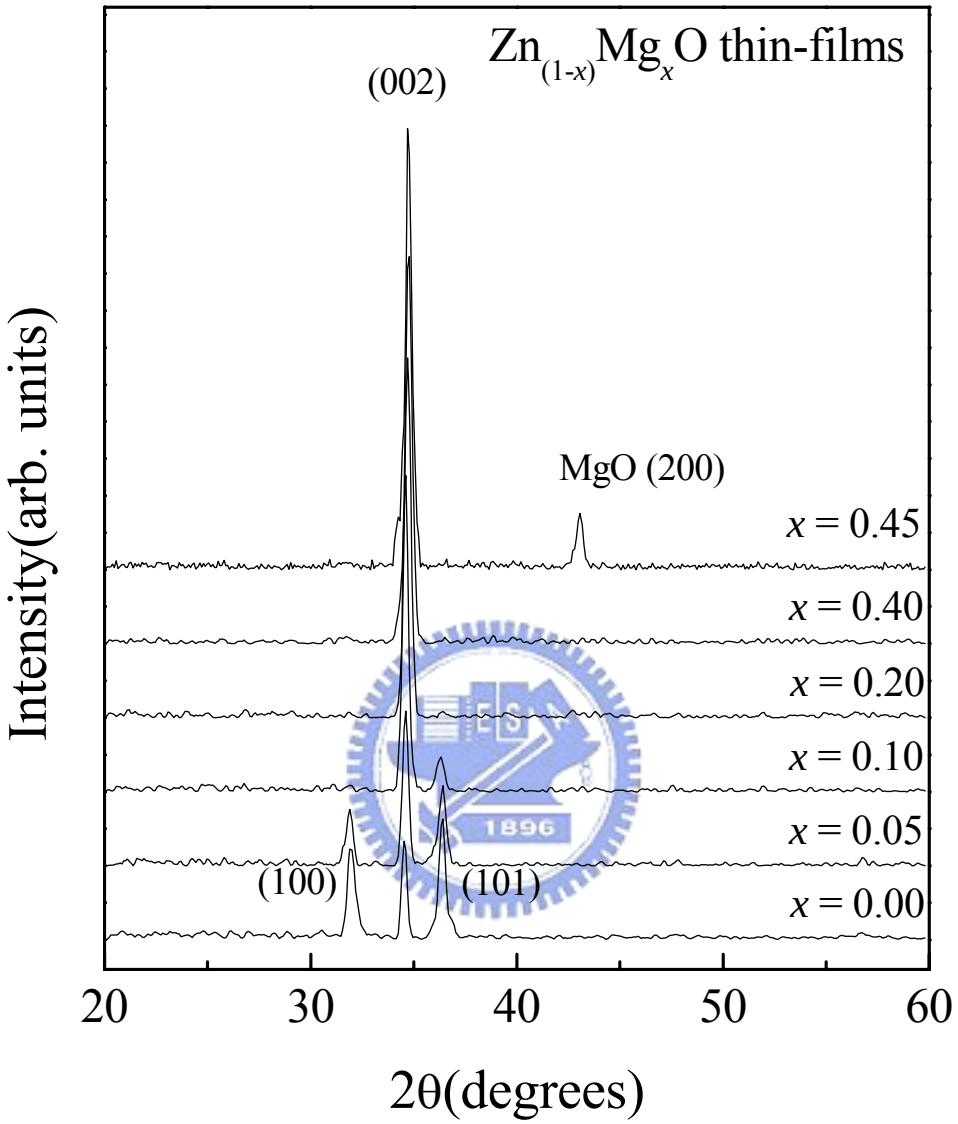

Figure 3-2 XRD patterns of $Zn_{(1-x)}Mg_xO$ films after annealing at 500°C for 2 hr.

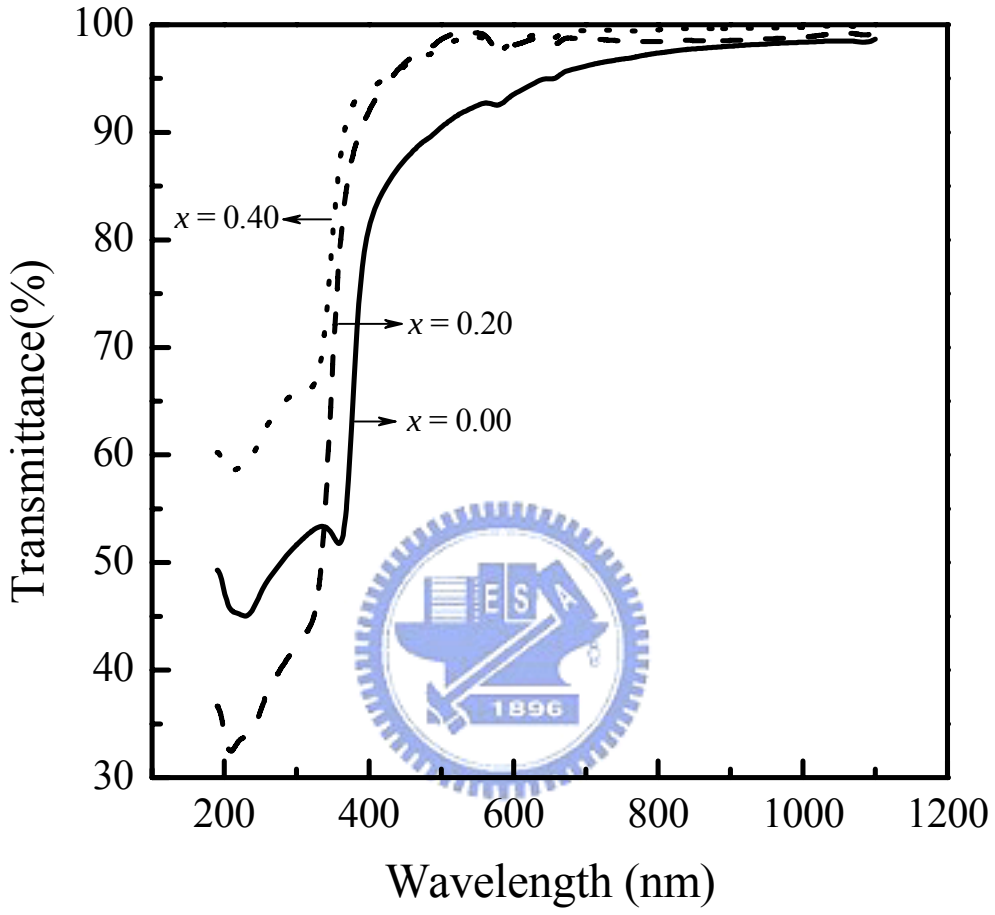

Figure 3-3 Transmittance spectra of $Zn_{(1-x)}Mg_xO$ films deposited on glass substrates.

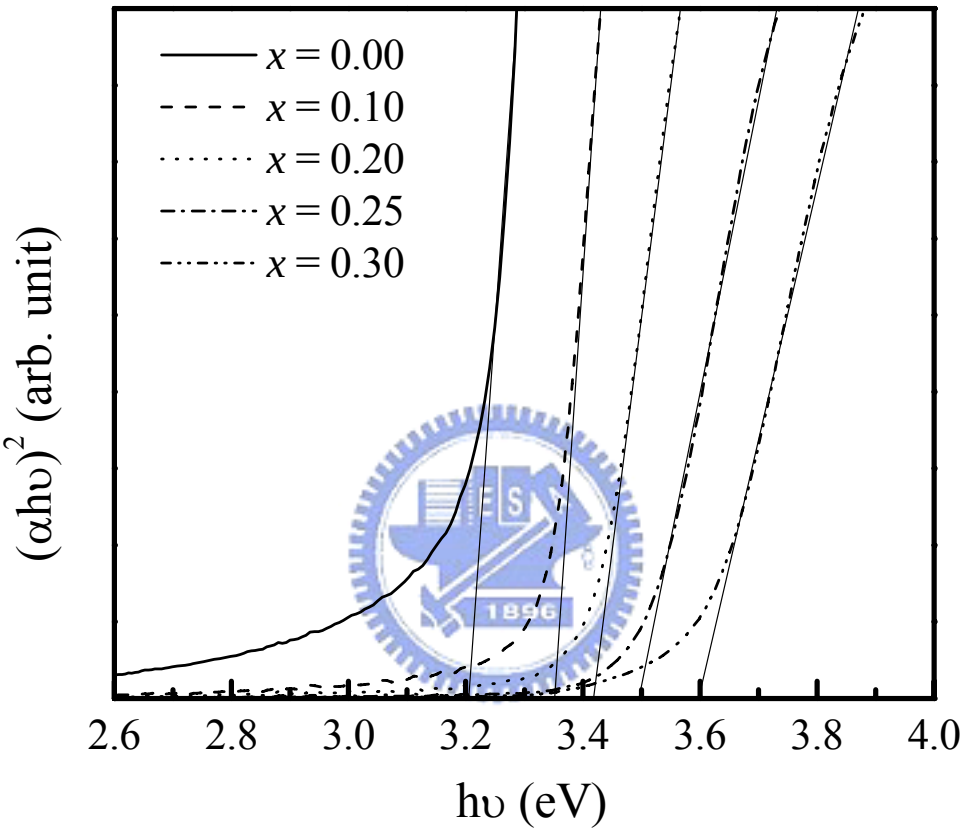

Figure 3-4 Relative absorption coefficients of the $Zn_{(1-x)}Mg_xO$ thin films, where *x* ranged form 0.00 to 0.30.

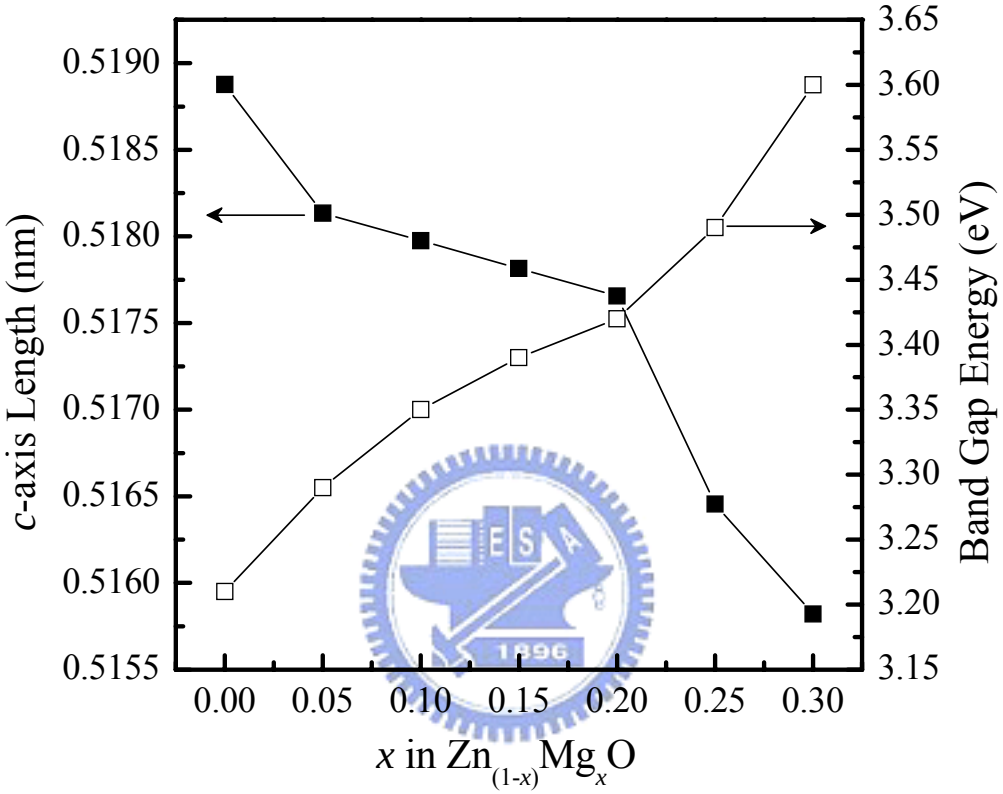

Figure 3-5 *c*-axis length and band gap energies of $Zn_{(1-x)}Mg_xO$ thin films, where *x* ranged form 0 to 0.30.

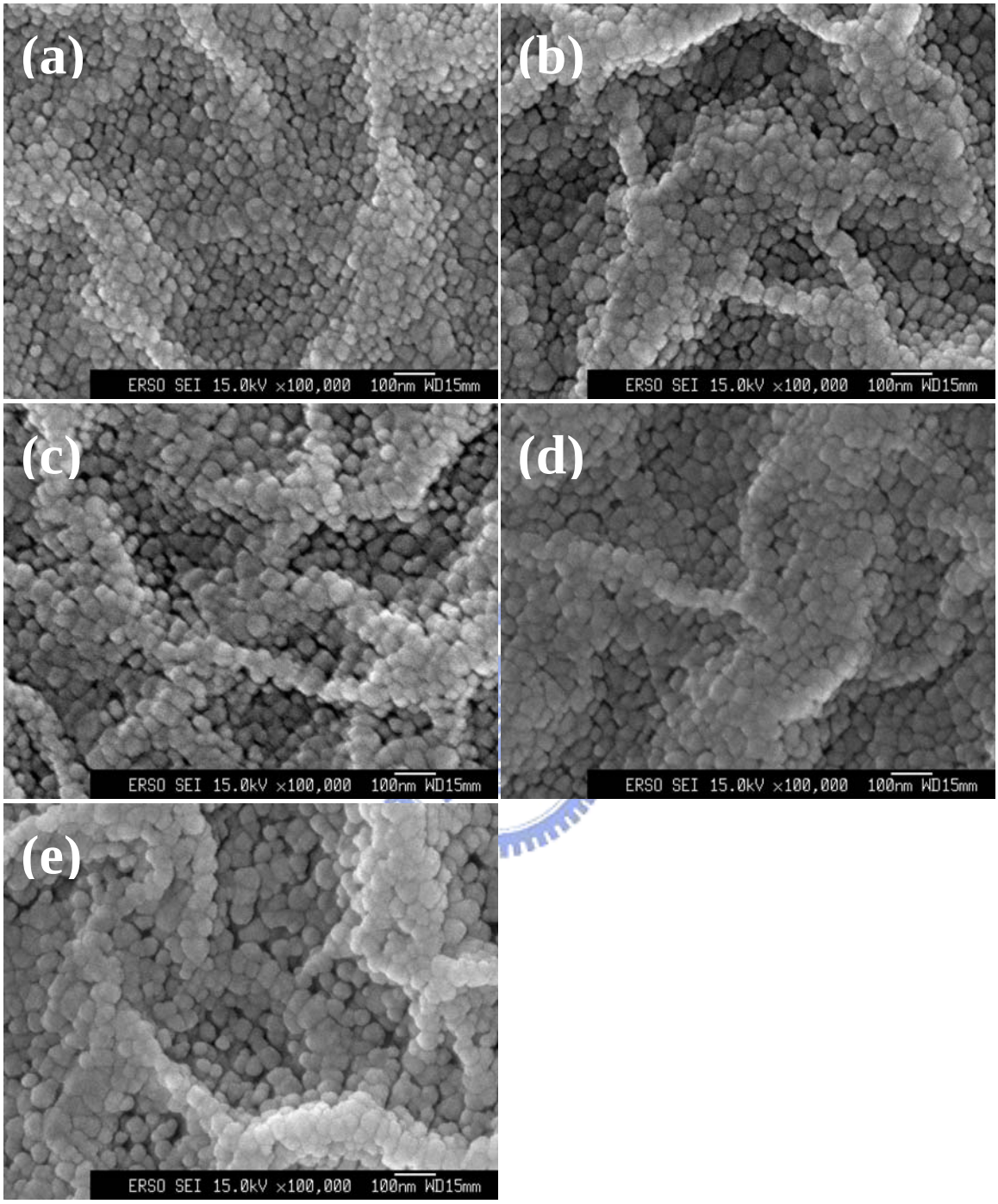

Figure 3-6 SEM images of un-doped ZnO thin films annealed at (a) 400°C, (b) 450°C, (c) 500°C, (d) 550°C, and (e) 600°C.

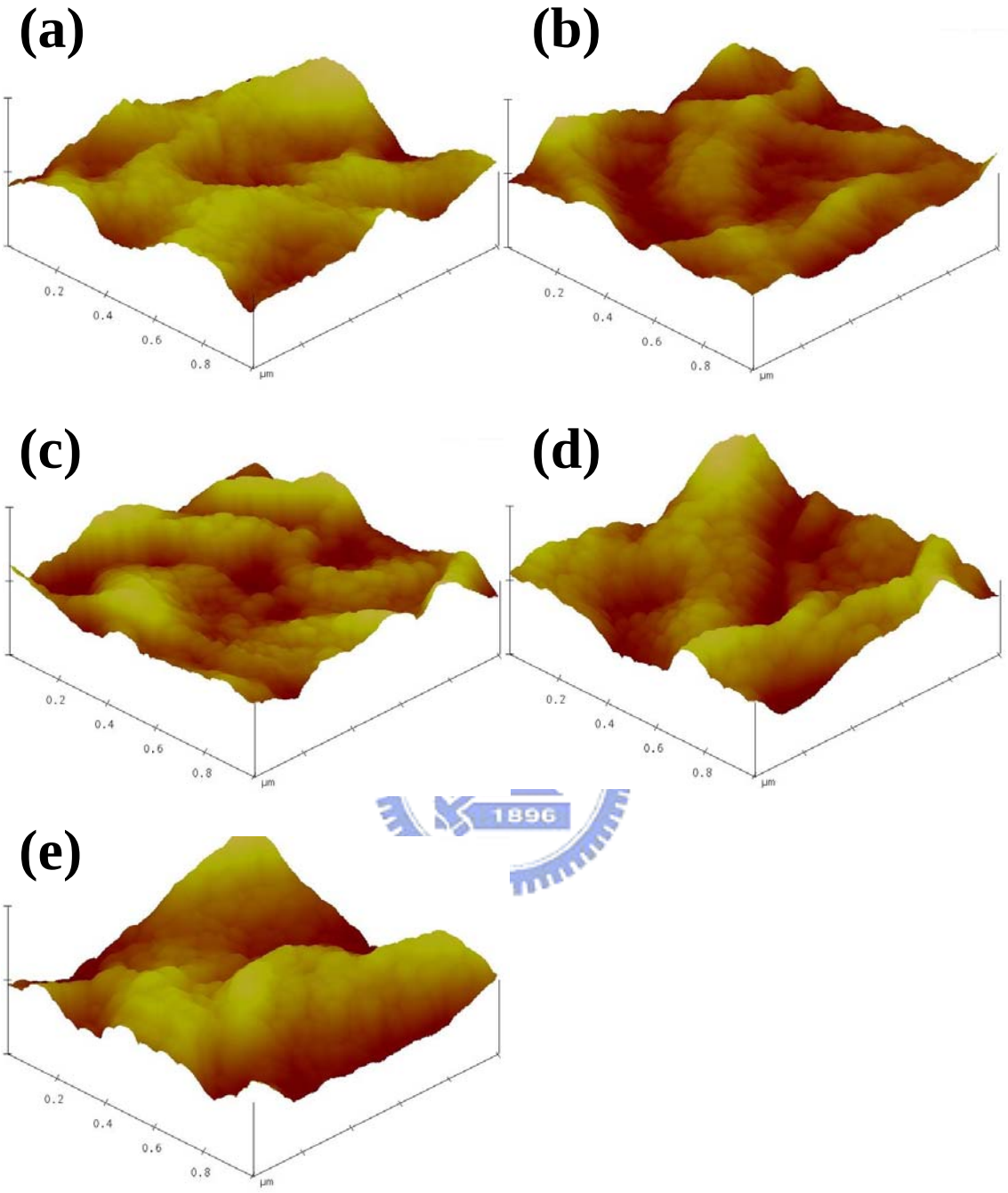

Figure 3-7 AFM surface observations of un-doped ZnO thin films annealed at (a) 400°C, (b) 450°C, (c) 500°C, (d) 550°C, and (e) 600°C.

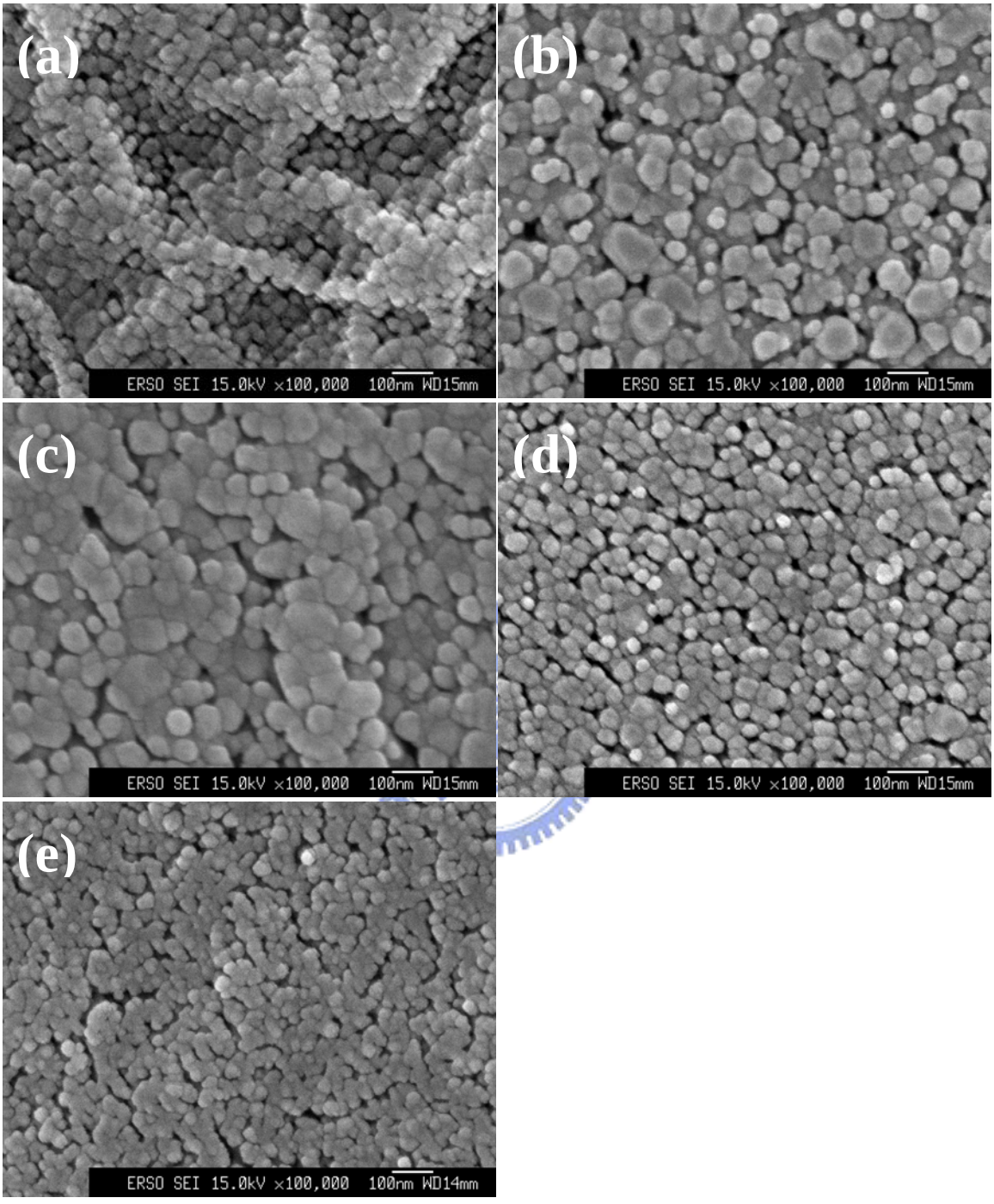

Figure 3-8 SEM images of $Zn_{(1-x)}Mg_xO$ thin films of (a) x = 0.00, (b) x = 0.10, (c) x = 0.20, (d) x = 0.30, and (e) x = 0.40.

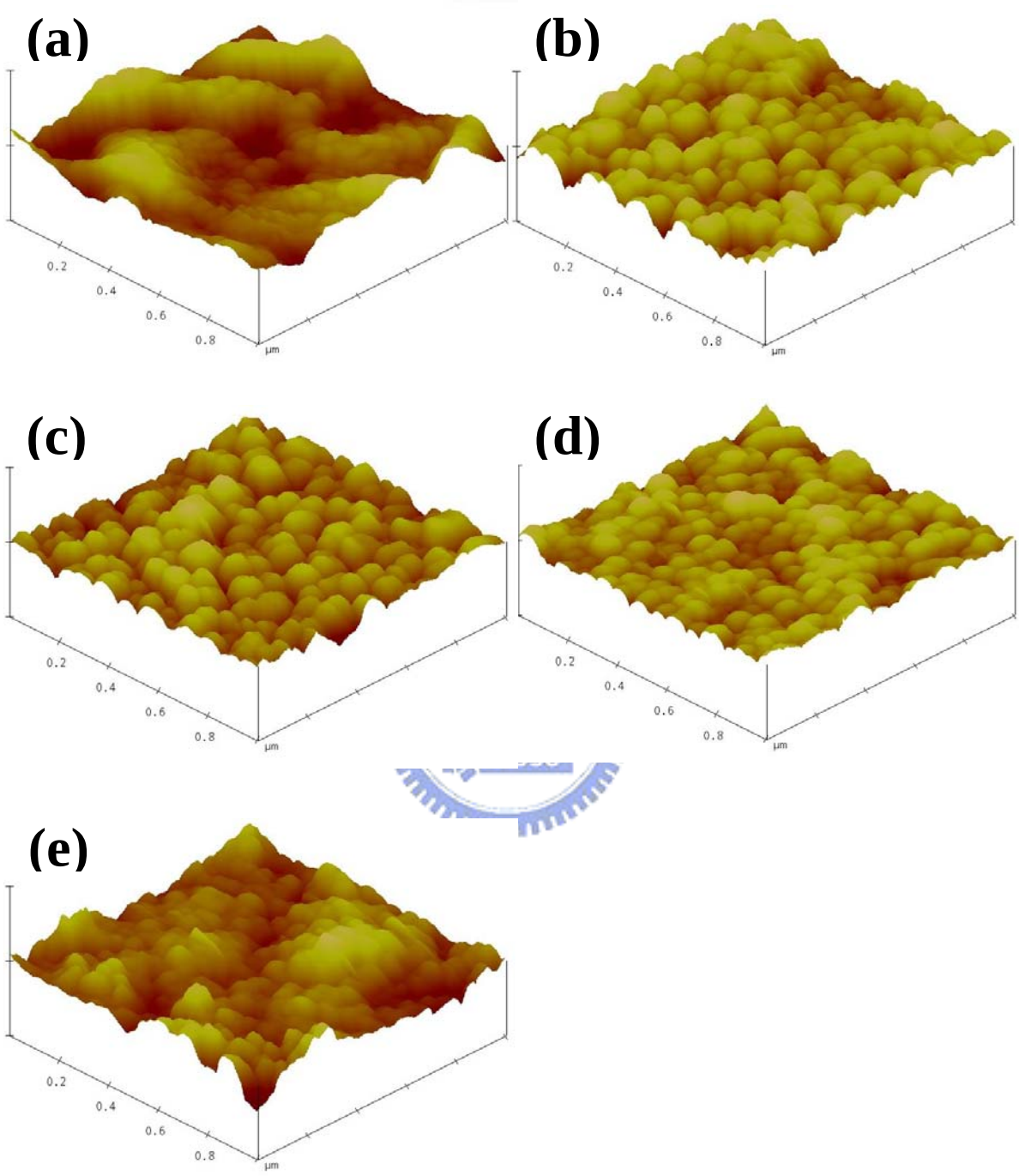

Figure 3-9 AFM surface observations of $Zn_{(1-x)}Mg_xO$ thin films of (a) x = 0.00, (b) x = 0.10, (c) x = 0.20, (d) x = 0.30, and (e) x = 0.40.

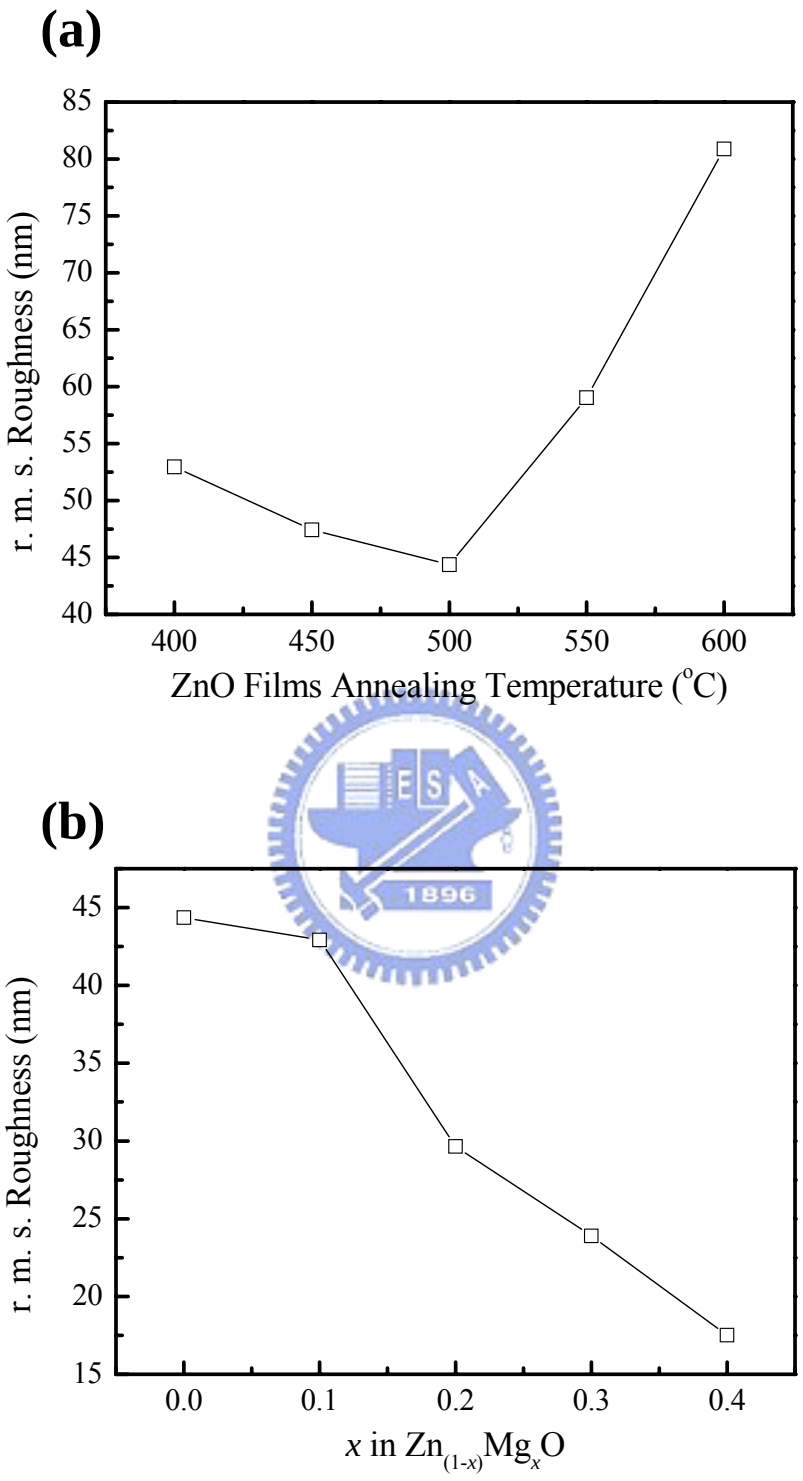

Figure 3-10 (a) Roughness of un-doped ZnO films annealed at various temperatures. (b) Roughness of $Zn_{(1-x)}Mg_xO$ films annealed at 500°C as a function of Mg content.

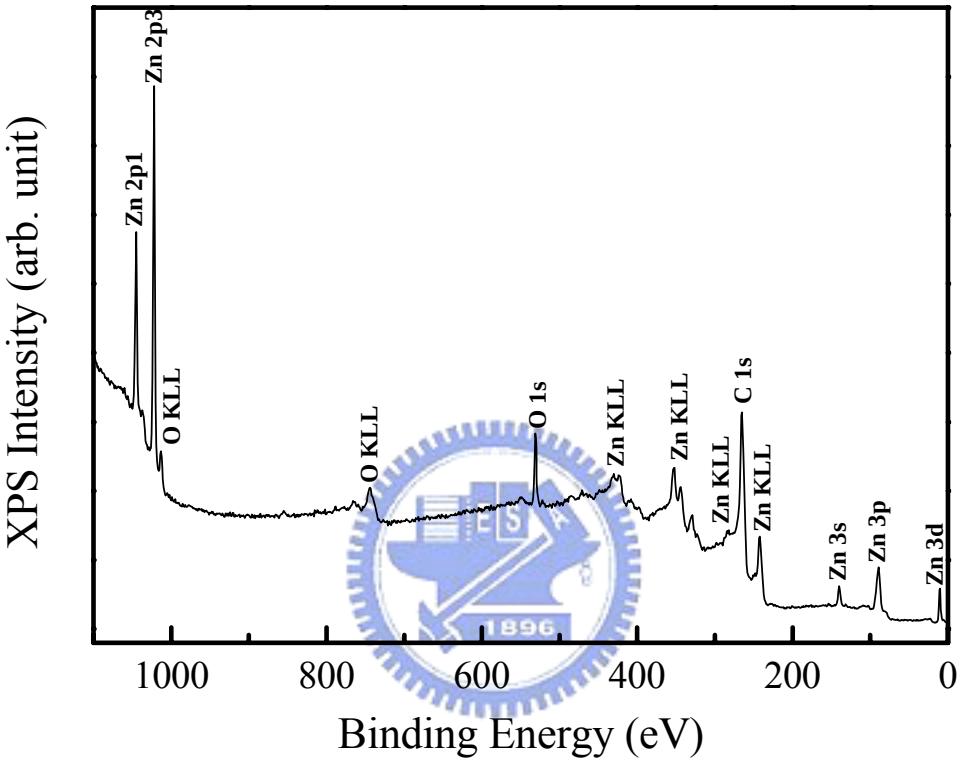

Figure 3-11 XPS survey scan analysis of un-doped ZnO thin film annealed at 500°C under air atmosphere for 2 hr.

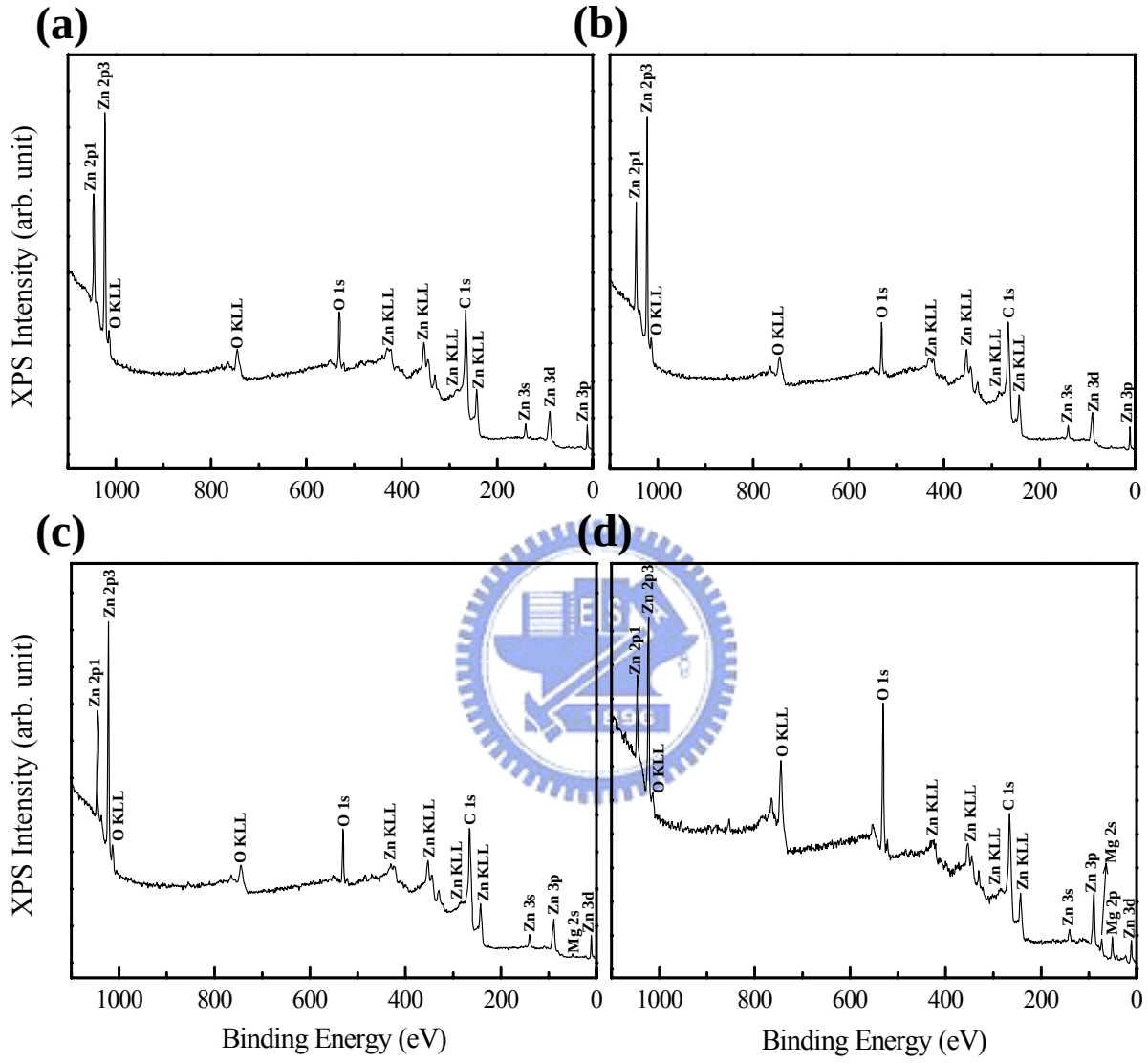

Figure 3-12 X-ray photoelectron spectroscopy survey scan analysis of $Zn_{(1-x)}Mg_xO$ thin films of (a) x = 0.10, (b) x = 0.20, (c) x = 0.30, and (d) x = 0.40.

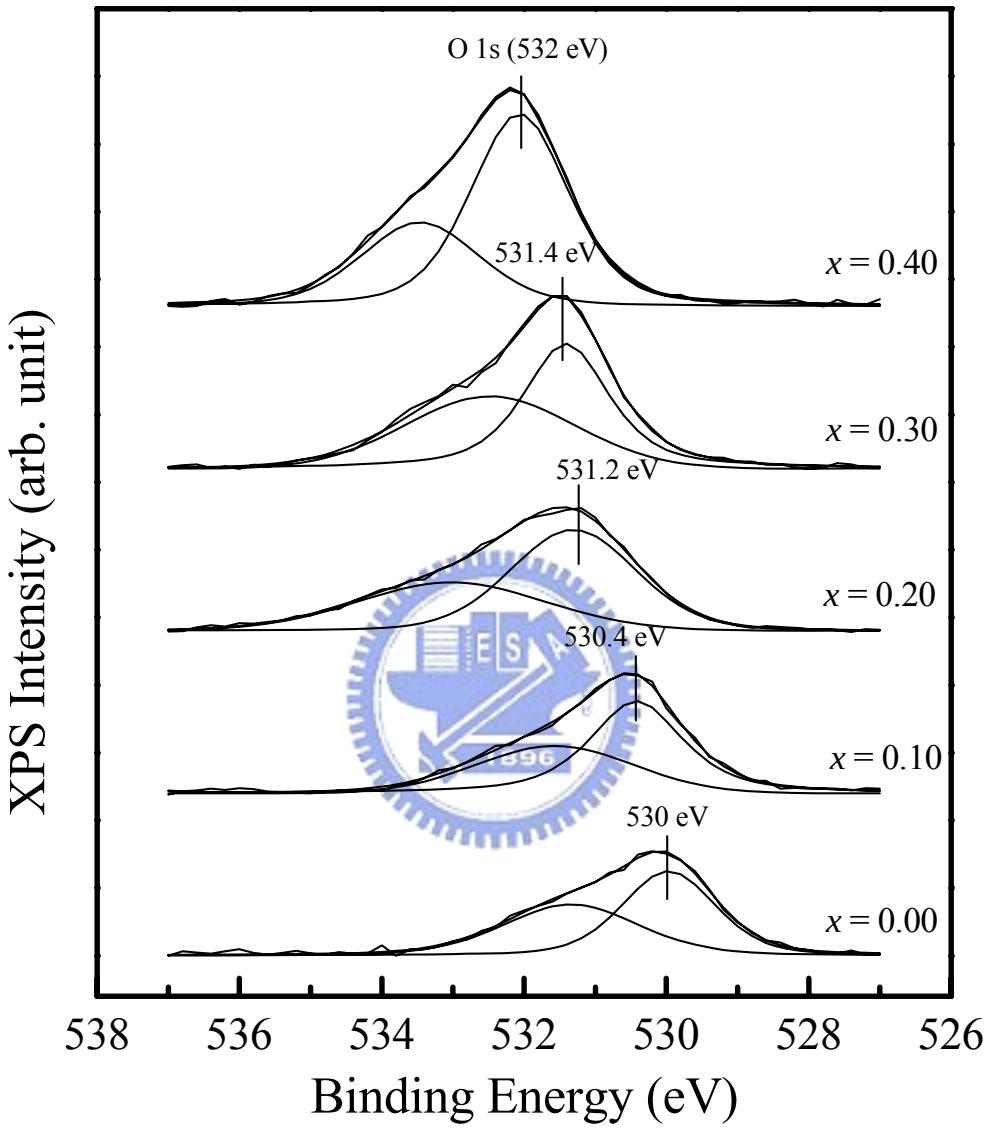

Figure 3-13 X-ray photoelectron spectroscopy spectra of O 1s of $Zn_{(1-x)}Mg_xO$ thin films, where *x* ranged from 0.00 to 0.40.

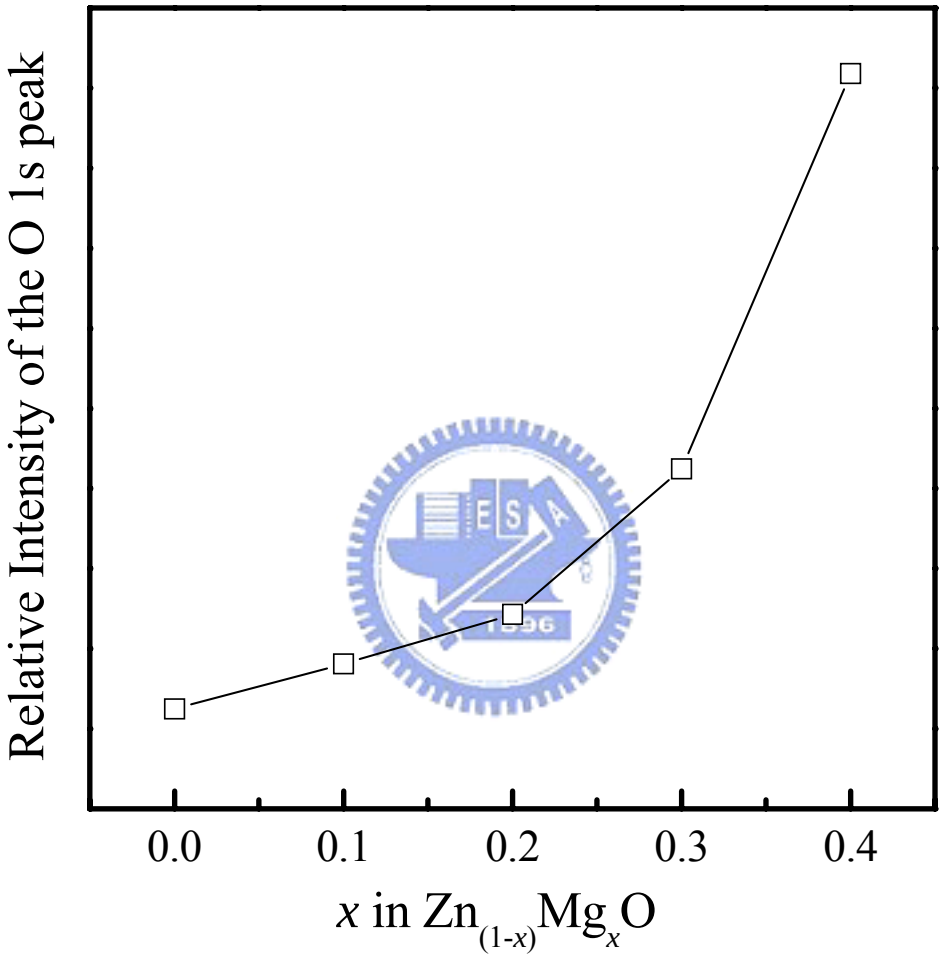

Figure 3-14 Dependence of relative intensity of the O 1s peak of the $Zn_{(1-x)}Mg_xO$ thin films, on the values of x.

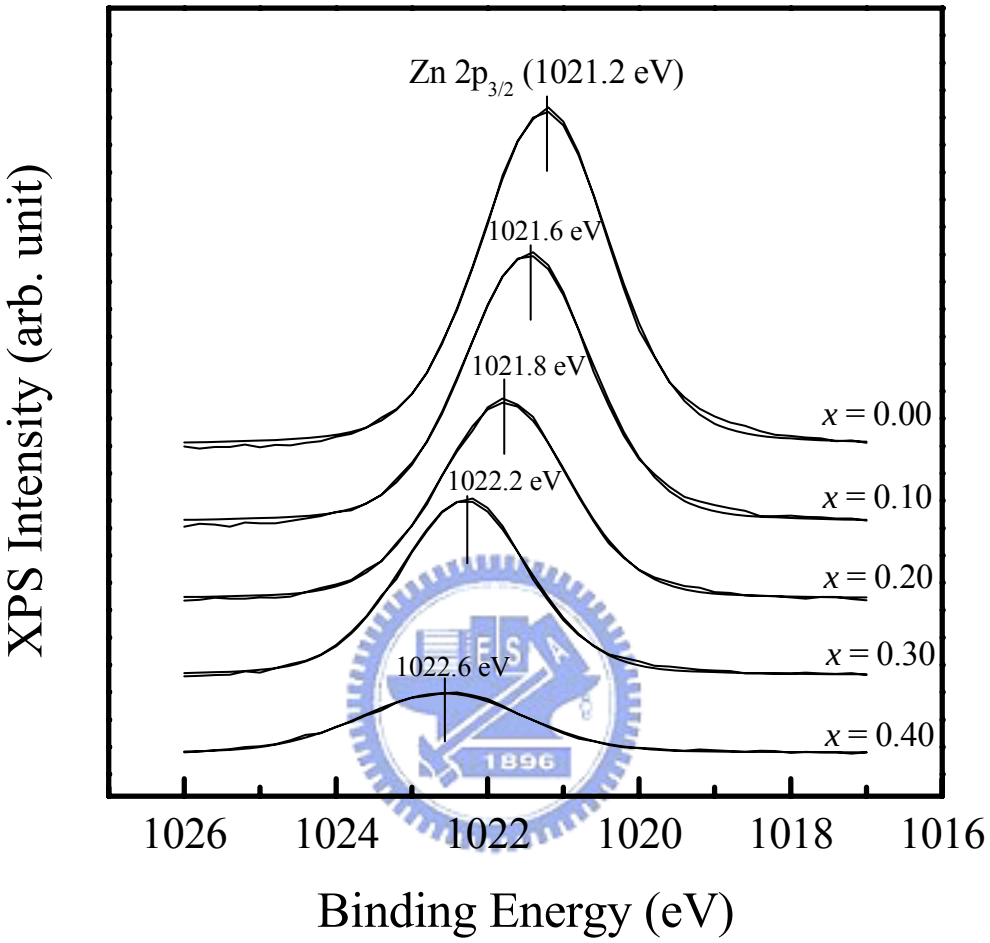

Figure 3-15 X-ray photoelectron spectroscopy spectra of Zn $2p_{3/2}$ of $Zn_{(1-x)}Mg_xO$ thin films, where *x* ranged from 0.00 to 0.40.

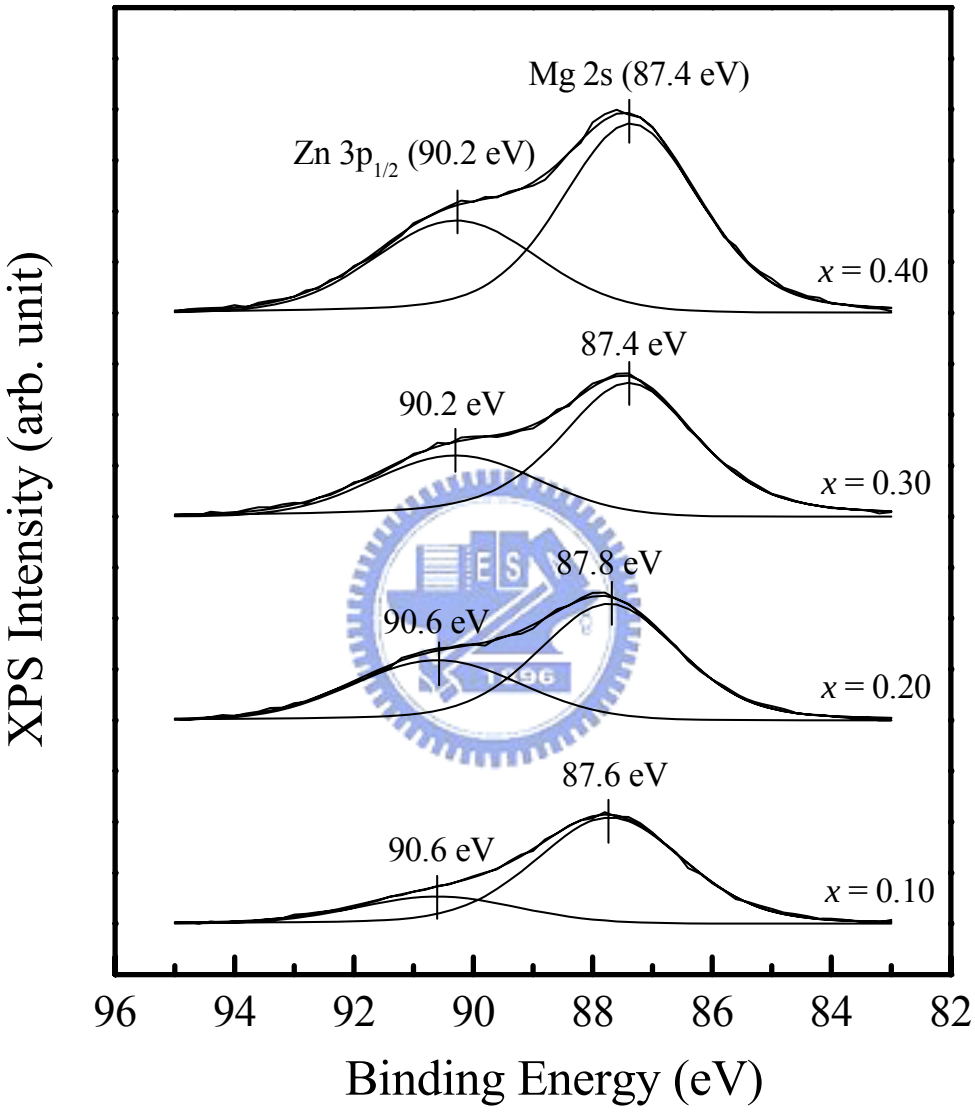

Figure 3-16 X-ray photoelectron spectroscopy spectra of Mg 2s and Zn $3p_{1/2}$ of $Zn_{(1-x)}Mg_xO$ thin films, where x ranged from 0.10 to 0.40.

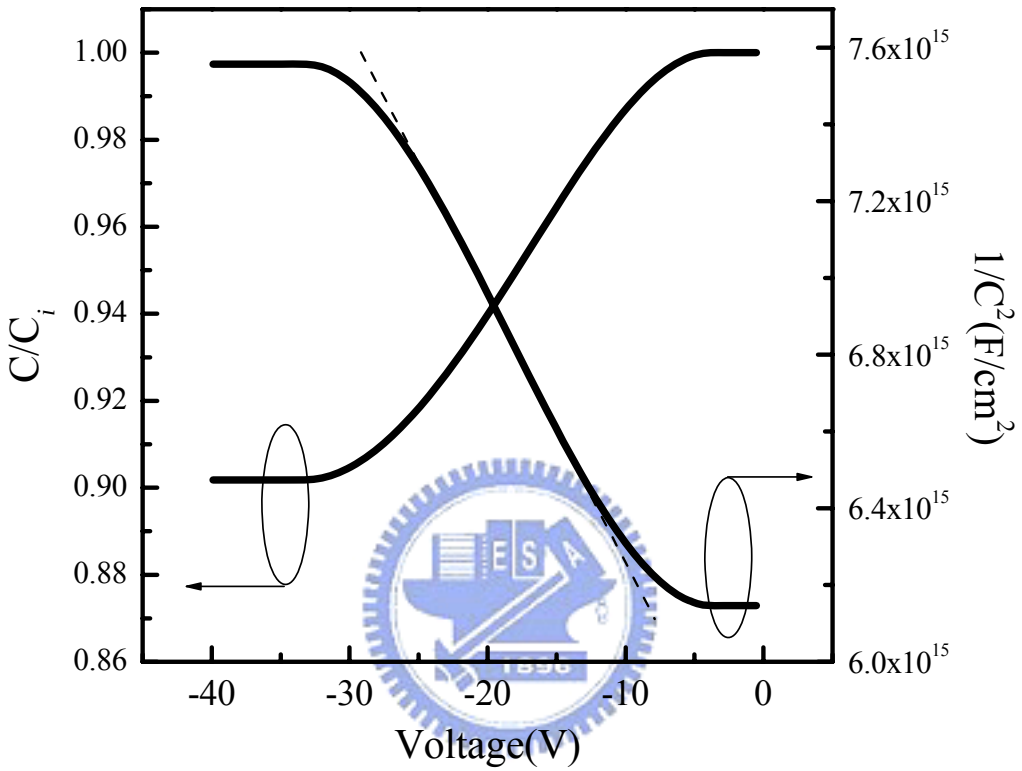

Figure 3-17 *C-V* curves obtained for MOS structure Al/SiO_2/ZnO (25°C). The charge carrier density *n* of the ZnO films was evaluated from the slope of C^{-2} vs *V*.

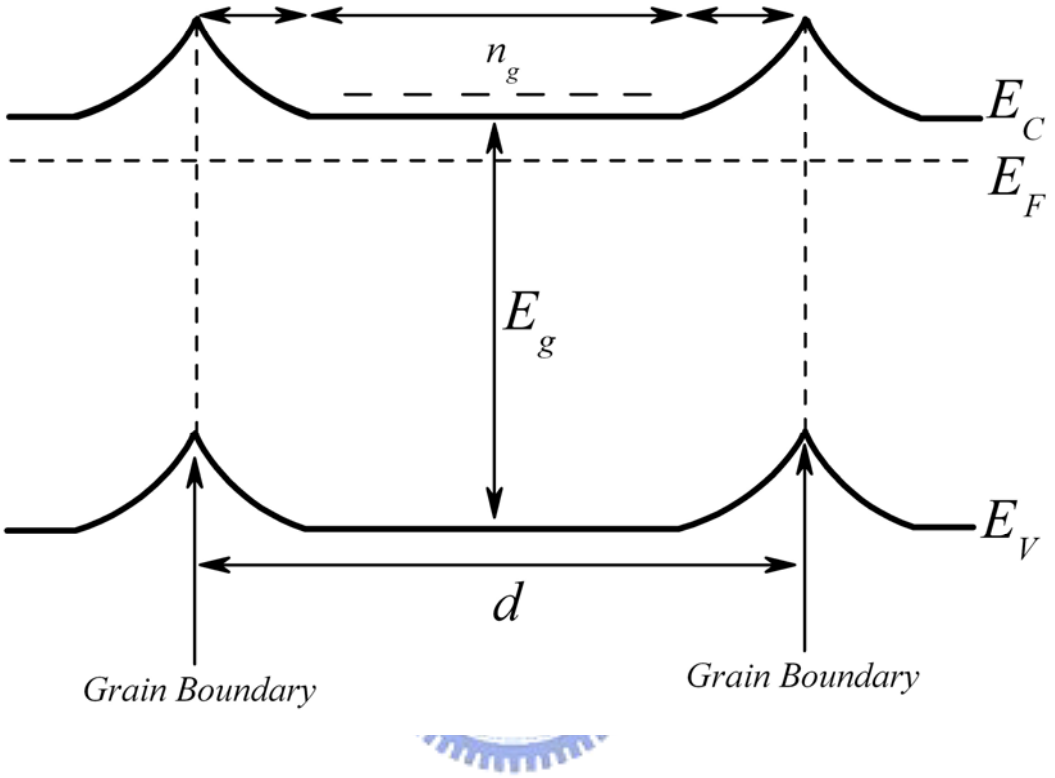

Figure 3-18 Energy band diagram of the double Schottky barrier of the $Zn_{(1-x)}Mg_xO$ thin films. All energy levels are referenced to the minimum energy level $E_V = 0$ and the maximum energy level E_{vac}.

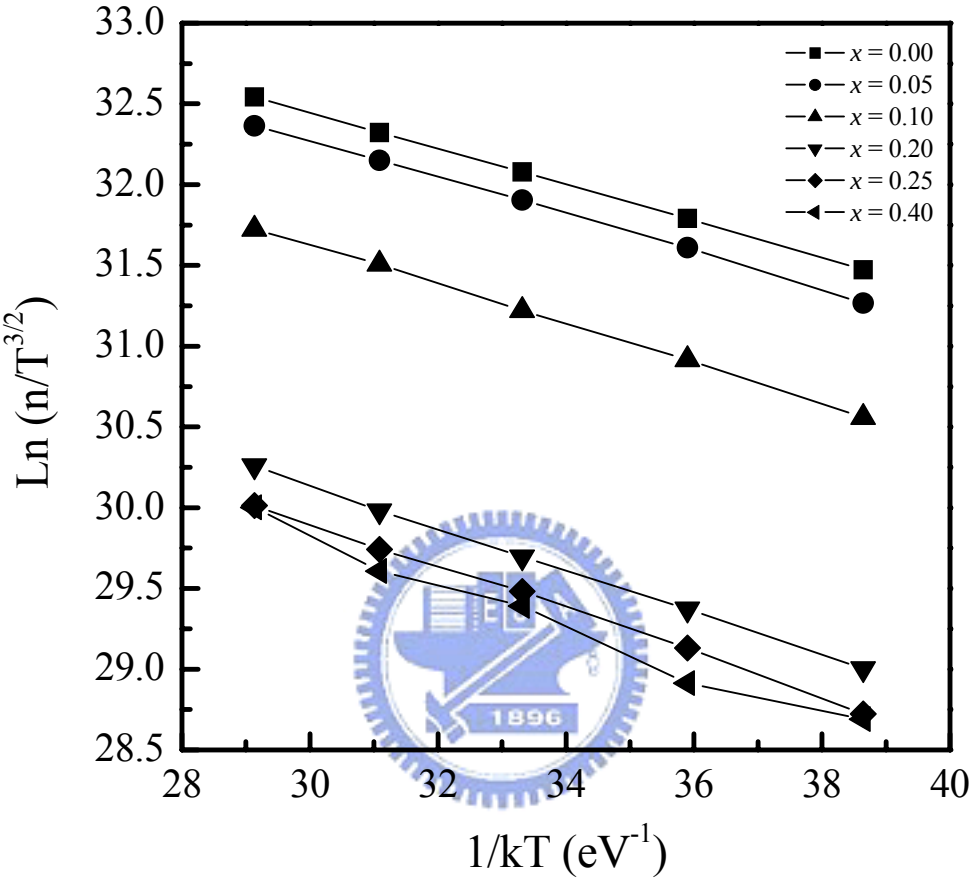

Figure 3-19 Plot of $\ln(n/T^{3/2})$ vs. $1/kT$, where n is the measured electron concentration in the $Zn_{(1-x)}Mg_xO$ films, showing a constant Fermi level within the temperature range 25~125°C.

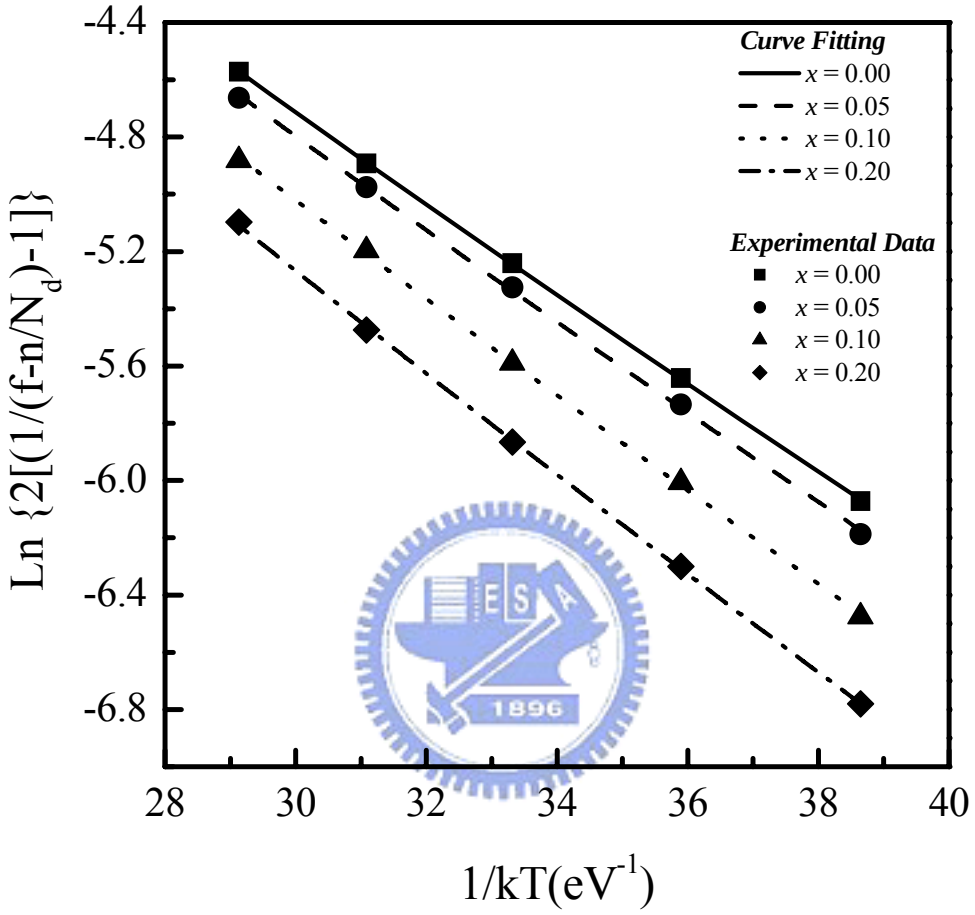

Figure 3-20 Plot of $\ln\{2/[f-n/rN_d]-2\}$ vs. $1/kT$. The constant slope (=E_d-E_F) shows a definite donor level below the Fermi level in the $Zn_{(1-x)}Mg_xO$ films.

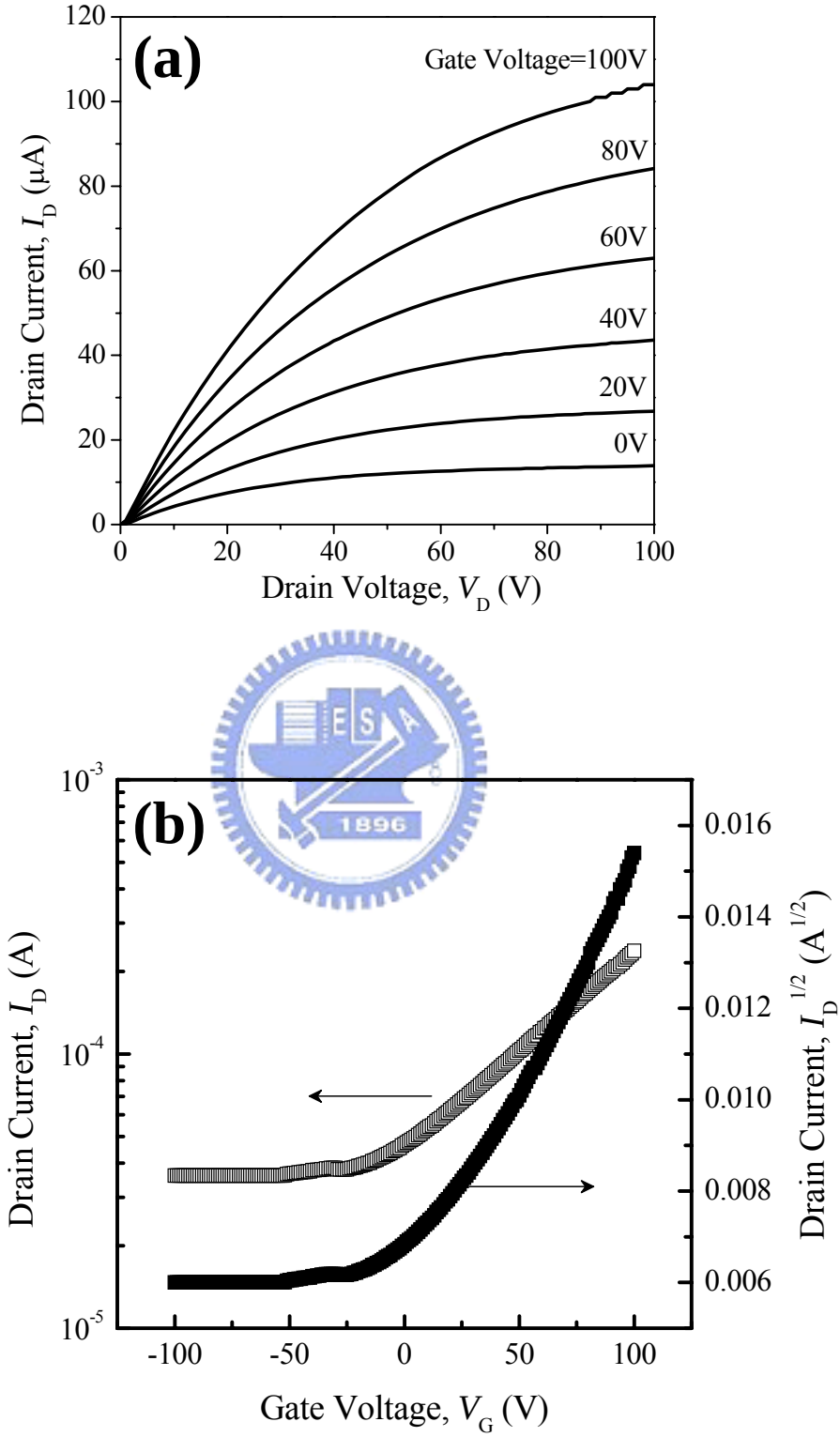

Figure 3-21 (a) Output and (b) transfer characteristics of the un-doped ZnO thin film transistor, recorded at a value of V_D of 100 V.

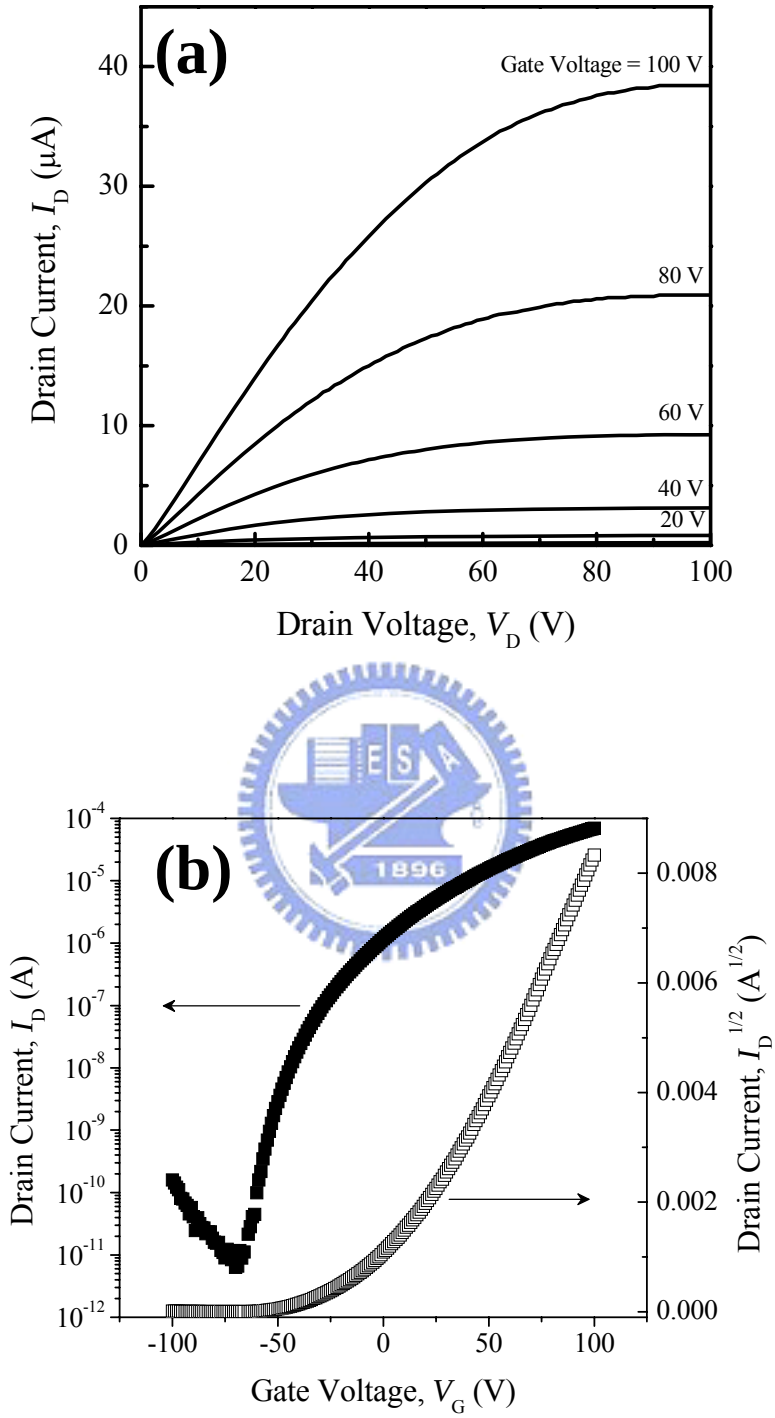

Figure 3-22 (a) Output and (b) transfer characteristics of $Zn_{(1-x)}Mg_xO$ thin film transistor, where x = 0.20, recorded at a value of V_D of 100 V.

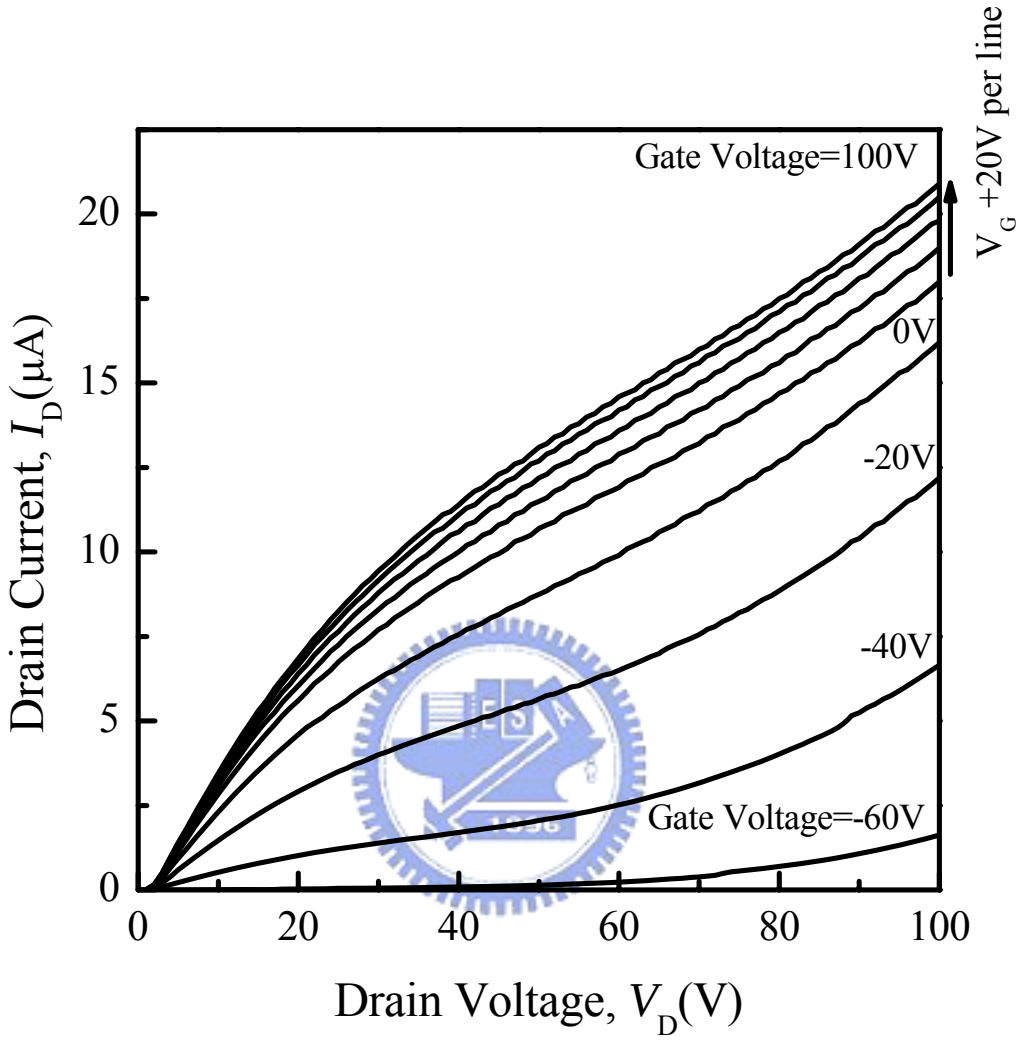

Figure 3-23 Output characteristics of $Zn_{(1-x)}Mg_xO$ TFTs of x = 0.25.

Table 3-1 Dielectric constant ε_s, carrier concentration at room temperature n_{RT}, Fermi energy level E_F, donor energy level E_d, the value of $rm_e^{3/2}$ and rN_d, the normalized ratios of r (R_r) and N_d (R_d) of $Zn_{(1-x)}Mg_xO$ thin films.

x	ε_s	n_{RT} ($\times10^{16}cm^{-3}$)	E_F(eV)	E_d(eV)	$rm_e^{3/2}$	rN_d ($\times10^{19}cm^{-3}$)	R_r	R_d
0.00	8.90	24.2	-0.112	-0.270	0.740	21.0	1.0	1.0
0.05	8.95	19.7	-0.115	-0.275	0.675	19.2	0.68	1.3
0.10	9.17	9.70	-0.123	-0.291	0.449	12.7	0.23	2.7
0.20	9.30	2.05	-0.131	-0.306	0.128	3.61	0.02	8.2

Table 3-2 Electrical characteristics (saturation mobility μ_{sat}, threshold voltage V_{th}, off-state current I_{off} and current modulation) of $Zn_{(1-x)}Mg_xO$ thin film transistors.

x in $Zn_{(1-x)}Mg_xO$	$\mu_{sat}(cm^2/Vs)$	$V_{th}(V)$	$I_{off}(A/\mu m)$	I_{on}/I_{off}
0.00	0.40	-31.9	6.93×10^{-7}	<10
0.05	0.37	-22.8	4.54×10^{-9}	5.11×10^{2}
0.10	0.28	-17.5	3.17×10^{-10}	6.77×10^{3}
0.15	0.21	-4.31	9.69×10^{-11}	2.14×10^{4}
0.20	0.24	7.75	2.34×10^{-13}	5.93×10^{6}
0.25	0.10	11.4	5.64×10^{-9}	1.43×10^{2}